NAVAL POSTGRADUATE SCHOOL
Monterey, California

THESIS

BEDFORM EVOLUTION UNDER THE COMBINED INFLUENCES OF WAVES AND CURRENTS AT THE INNER-SHELF MISO SITE

by

William C. Blodgett, Jr.

June 2002

Thesis Advisor: Timothy P. Stanton
Second Reader: Edward B. Thornton

Approved for public release; distribution is unlimited.

THIS PAGE INTENTIONALLY LEFT BLANK

REPORT DOCUMENTATION PAGE			Form Approved OMB No. 0704-0188
Public reporting burden for this collection of information is estimated to average 1 hour per response, including the time for reviewing instruction, searching existing data sources, gathering and maintaining the data needed, and completing and reviewing the collection of information. Send comments regarding this burden estimate or any other aspect of this collection of information, including suggestions for reducing this burden, to Washington headquarters Services, Directorate for Information Operations and Reports, 1215 Jefferson Davis Highway, Suite 1204, Arlington, VA 22202-4302, and to the Office of Management and Budget, Paperwork Reduction Project (0704-0188) Washington DC 20503.			
1. AGENCY USE ONLY *(Leave blank)*	**2. REPORT DATE** June 2000	**3. REPORT TYPE AND DATES COVERED** Master's Thesis	
4. TITLE AND SUBTITLE: Title (Mix case letters) Bedform Evolution Under the Combined Influences of Waves and Currents at the Inner-Shelf MISO Site			**5. FUNDING NUMBERS**
6. AUTHOR(S) Blodgett, William C.			
7. PERFORMING ORGANIZATION NAME(S) AND ADDRESS(ES) Naval Postgraduate School Monterey, CA 93943-5000			**8. PERFORMING ORGANIZATION REPORT NUMBER**
9. SPONSORING /MONITORING AGENCY NAME(S) AND ADDRESS(ES) N/A			**10. SPONSORING/MONITORING AGENCY REPORT NUMBER**
11. SUPPLEMENTARY NOTES The views expressed in this thesis are those of the author and do not reflect the official policy or position of the Department of Defense or the U.S. Government.			
12a. DISTRIBUTION / AVAILABILITY STATEMENT Approved for public release; distribution is unlimited.			**12b. DISTRIBUTION CODE**

13. ABSTRACT ***(maximum 200 words)***

Observations of the temporal evolution of waves, currents, and bed response data collected by an instrumented frame deployed in 12m of water at the Monterey Inner Shelf Observatory (MISO) off the coast of Monterey, California are analyzed in terms of measured wave and current forcing statistics and ripple geometry. During the year 2000, a Broadband Acoustic Doppler Current Profiler (BADCP) collected continuous wave and current measurements. Bed morphology was continually mapped by a Scanning Acoustic Altimeter (SAA) in a 1m alongshore by 1.5m cross-shore area immediately offshore from the MISO frame. Relict ripples were observed to dominate the bedforms throughout much of the year. Ripple growth in the alongshore direction was observed during conditions of marginally critical flow as defined by the critical combined wave and current Shields parameter. As flow conditions increased above the critical level, ripple growth in the alongshore direction ceased, and cross-shore wavelengths began to grow and dominate. Together, these observations and data sets are used to evaluate the applicability of existing ripple prediction algorithms. Altogether, five models are tested, and it was concluded that they could not independently predict the bed's response.

14. SUBJECT TERMS Oceanography, Nearshore, Ripples, Bedform Evolution, Waves, Currents, Sediment Transport			**15. NUMBER OF PAGES** 95
			16. PRICE CODE
17. SECURITY CLASSIFICATION OF REPORT Unclassified	**18. SECURITY CLASSIFICATION OF THIS PAGE** Unclassified	**19. SECURITY CLASSIFICATION OF ABSTRACT** Unclassified	**20. LIMITATION OF ABSTRACT** UL

NSN 7540-01-280-5500 Standard Form 298 (Rev. 2-89)
Prescribed by ANSI Std. 239-18

THIS PAGE INTENTIONALLY LEFT BLANK

Approved for public release; distribution is unlimited.

BEDFORM EVOLUTION UNDER THE COMBINED INFLUENCES OF WAVES AND CURRENTS AT THE INNER-SHELF MISO SITE

William C. Blodgett, Jr.
Ensign, United States Navy
B.S., United States Naval Academy, 2001

Submitted in partial fulfillment of the
requirements for the degree of

MASTER OF SCIENCE IN PHYSICAL OCEANOGRAPHY

from the

NAVAL POSTGRADUATE SCHOOL
June 2002

Author: William C. Blodgett, Jr.

Approved by: Timothy P. Stanton
Thesis Advisor

Edward B. Thornton
Second Reader

Mary L. Batteen
Chairman, Department of Oceanography

THIS PAGE INTENTIONALLY LEFT BLANK

ABSTRACT

Observations of the temporal evolution of waves, currents, and bed response data collected by an instrumented frame deployed in 12m of water at the Monterey Inner Shelf Observatory (MISO) off the coast of Monterey, California are analyzed in terms of measured wave and current forcing statistics and ripple geometry. During the year 2000, a Broadband Acoustic Doppler Current Profiler (BADCP) collected continuous wave and current measurements. Bed morphology was continually mapped by a Scanning Acoustic Altimeter (SAA) in a 1m alongshore by 1.5m cross-shore area immediately offshore from the MISO frame. Relict ripples were observed to dominate the bedforms throughout much of the year. Ripple growth in the alongshore direction was observed during conditions of marginally critical flow as defined by the critical combined wave and current Shields parameter. As flow conditions increased above the critical level, ripple growth in the alongshore direction ceased, and cross-shore wavelengths began to grow and dominate. Together, these observations and data sets are used to evaluate the applicability of existing ripple prediction algorithms. Altogether, five models are tested, and it was concluded that they could not independently predict the bed's response.

THIS PAGE INTENTIONALLY LEFT BLANK

TABLE OF CONTENTS

THIS PAGE INTENTIONALLY LEFT BLANK

LIST OF FIGURES

THIS PAGE INTENTIONALLY LEFT BLANK

LIST OF TABLES

THIS PAGE INTENTIONALLY LEFT BLANK

ACKNOWLEDGMENTS

Professor Stanton was an outstanding mentor who introduced me to the world of nearshore oceanography. He provided invaluable guidance and instruction throughout my entire graduate experience, and I wish to thank him for this support of my research endeavors. This project could not have been completed without his patience and high standards of excellence.

I would also like to thank Dr. Thornton, my second-reader, for his professional advice and continued interest in my scientific development. He provided excellent insight into the nearshore environment, and has inspired me to pursue future education in the field of oceanography.

In addition, this study would not have been possible without the technical expertise of several individuals including: Dr. Reniers for his assistance with the wave directional spectra, Jim Stockel and Mike Cooke for their programming expertise, and Rob Wyland for his aid in understanding wave directional spectra and the engineering of MISO.

Lastly, I must credit my family and friends for their steadfast support of my professional development at the Naval Postgraduate School both as a military officer, and as a scientist. Their encouragement and interest in my well-being helped to sustain me through even the most difficult of times.

THIS PAGE INTENTIONALLY LEFT BLANK

I. INTRODUCTION

Bottom bedforms develop on sandy beds in shallow coastal waters along the inner continental self in response to flows of water of sufficient strength to mobilize the sediment. As these bedforms develop and ripples are created, the bottom roughness changes, altering the structure of the turbulent bottom boundary layer. Thus, ripple formation has a significant impact on bed stress, wave dissipation rates, near bed velocity structure, and the amount of sediment suspended in the water column [*Grant and Madsen*, 1982]. To better understand the bottom boundary layer hydrodynamics and sediment transport, the bottom geometry of mobile, sandy beds as a function of flow and sediment parameters must be characterized.

Numerous laboratory and field studies have been conducted to determine relationships between wave forcing, grain size, and ripple geometry. Most of these studies have focused on wave-formed ripples typical of confined shallow water environments where wave stresses dominate over those caused by mean currents. Laboratory studies pioneered by *Bagnold* [1946] and continued by *Yalin and Russell* [1962], *Mogridge and Kamphuis* [1972], and *Miller and Komar* [1980a], among others, have sought empirical formulae to classify the size and shape of sand ripples using a variety of experimental devices including flumes, water tunnels, oscillatory beds, using different sediment sizes and densities.

Bagnold [1946] originally classified wave-generated ripples into two categories: rolling grain ripples and vortex ripples. Rolling grain ripples formed as sand grains began to move and align with each other in ridges perpendicular to gentle oscillatory flow. Once the flow velocity increased to twice that of the onset of sediment motion, a vortex formed on the lee side of the ridge. This vortex moved sand from the lee-side trough to the crest, effectively increasing the ripple steepness, and creating vortex ripples. Like rolling grain ripples, the length of the vortex ripples grew until equilibrium was reached with the wave orbital diameter, or washed out as the wave stress reached sheet flow conditions. *Bagnold* [1946] concluded that vortex ripples were the primary bed response in strongly forced, high sediment transport flow conditions.

Bagnold's 1946 experiments and other laboratory studies are limited by the level of wave conditions generated. Small-scale laboratory equipment cannot adequately reproduce long period, high energy wave conditions often experienced in the field. Wave-dominated field studies conducted by *Dingler* [1974] and *Miller and Komar* [1980b] took into account a wide range of wave heights and periods. Field studies such as these are complicated when the wave field is broadbanded with directional spreading, making relationships between wave conditions and measured ripple geometry more difficult to ascertain. In addition, due to the complexities of obtaining concurrent measurements of wave and bed characteristics, field studies are often short in duration and only marginally measure the bedforms.

To gain a more complete understanding of the bed's response to wave forcing, *Nielsen* [1981] combined the findings of laboratory and field studies to model ripple geometry in wave-dominated environments. He developed separate expressions for laboratory and field conditions, obtaining formulae for ripple wavelength (l), height (h), and steepness (h/l). For laboratory data, he obtained the ripple wavelength relationship

$$l / a = 2.2 - 0.345 y_w^{-0.34} \tag{1}$$

where a is the water semi-excursion amplitude, and y_w is the wave mobility number defined by

$$y_w = (aw)^2 / (s-1)gD \tag{2}$$

w is the radian frequency (2π/T, where T is the wave period), s is the relative sediment density, D is the mean grain diameter, and g is the gravity acceleration constant. *Nielsen's* [1981] laboratory derived ripple height calculation is

$$h / a = 0.275 - 0.022\sqrt{y_w} \tag{3}$$

and his ripple steepness formula is

$$h / l = 0.182 - 0.24 q^{1.5} \tag{4}$$

where the Shields parameter q is equal to one half the mobility number multiplied by *Jonsson's* [1967] wave friction factor.

For field data, *Nielsen* [1981] concluded that the ripple wavelength, height, and steepness for quartz sand had the following relationships

$$l / a = \exp\left(\frac{693 - 0.37 \ln^7 y_w}{1000 + 0.75 \ln^8 y_w} \right) \tag{5}$$

$$h / a = 21 y_w^{-1.85} \tag{6}$$

$$h / l = 0.342 - 0.34 \sqrt[4]{q} \tag{7}$$

respectively.

In their evaluation of several wave-dominated field studies, *Clifton and Dingler* [1984] identified three categories of ripples: orbital, anorbital, and suborbital. Orbital ripples form when the ratio of wave orbital diameter (d_w) to grain size diameter (D) lies in the range of 100-3000. In this range, *Miller and Komar* [1980a] concluded that orbital ripple wavelength (λ_{orb}) is proportional to the wave orbital diameter according to

$$l_{orb} = 0.65 d_w \tag{8}$$

At large ratios with d_w/D (>5000), ripple spacing becomes nearly independent of wave orbital diameter. These ripples, called anorbital, are prevalent in fine sandy beds under long period waves and have ripple wavelengths which scale directly with a multiple of grain size [*Clifton and Dingler*, 1984]:

$$l_{ano} \approx 400D - 600D \tag{9}$$

In the transitional range between orbital and anorbital ripples, intermediate wavelength features called suborbital ripples develop. The relationship between ripple wavelength and wave orbital diameter / grain diameter of suborbital ripples varies.

Wiberg and Harris [1994] analyzed *Clifton and Dingler's* [1984] ripple classification system for both laboratory and field studies, and concluded that while short wave period laboratory equipment produces orbital ripples, ripple conditions on the continental shelf most often fall in the range of suborbital or anorbital. By analyzing several sets of laboratory and field ripple measurements, *Wiberg and Harris* [1994] provide different estimates of orbital and anorbital wavelength according to

$$l_{orb} = 0.62 d_w \tag{10}$$

$$l_{ano} = 535D \tag{11}$$

respectively. The average ripple steepness for orbital and anorbital ripples was determined according to the following two equations:

$$\left(\frac{h}{l}\right)_{orb} = 0.17 \tag{12}$$

$$\left(\frac{h}{l}\right)_{ano} = \exp\left[-0.095\left(\ln\frac{d_w}{h_{ano}}\right)^2 + 0.442\ln\frac{d_w}{h_{ano}} - 2.28\right] \qquad (13)$$

Wiberg and Harris [1994] contend that the ratio of wave orbital diameter to anorbital ripple height best classifies ripples into orbital, anorbital, and suborbital conditions according to the limits

$$d_w/h_{ano} < 20 \qquad \text{orbital ripples} \qquad (14a)$$

$$20 < d_w/h_{ano} < 100 \qquad \text{suborbital ripples} \qquad (14b)$$

$$d_w/h_{ano} > 100 \qquad \text{anorbital ripples} \qquad (14c)$$

While equations 10-13 classify ripple wavelength and steepness for orbital and anorbital cases, a suborbital wavelength predictor was derived using the boundaries established in equations 14(a) and 14(c):

$$l_{sub} = \exp\left[\left(\frac{\ln(d_w/h_{ano}) - \ln 100}{\ln 20 - \ln 100}\right)(\ln l_{orb} - \ln l_{ano}) + \ln l_{ano}\right] \qquad (15)$$

The underlying assumption in the *Nielsen* [1981] and *Wiberg and Harris* [1994] models is that the oscillatory flow component dominates at all times. This is not always true, as flows with both steady and oscillatory components are commonly present in the

continental shelf (most noticeably during storms [*Glenn and Grant*, 1987]), and can extend to the seafloor to add to the wave/oscillatory motion and effectively initiate sediment motion [*Grant and Madsen*, 1979]. *Clifton and Dingler* [1984] note that ripples become asymmetric in the direction of the mean current under oscillatory flow with axial mean currents.

Until recently, there have been few investigators of bedforms generated from combined wave and current flow. Laboratory studies conducted by *Grant and Madsen* [1979], *Glenn and Grant* [1987], and *Khelifa and Ouellet* [2000] as well as field studies by *Amos et al.* [1988] and *Li and Amos* [1998] all present empirical formulae for predicting ripple geometry under the combined actions of waves and currents. *Khelifa and Ouellet* [2000] conclude that empirical formulae used to model ripple wavelength and height for pure wave motion are not applicable for ripple prediction under combined waves and currents. *Khelifa and Ouellet* [2000] proceed to derive empirical formulae for ripple wavelength and height from laboratory produced ripple measurements. Their ripple wavelength equation for combined flow is

$$\frac{2l}{d_{cw}} = 1.9 + 0.08\ln^2\left(1+y_{wc}\right) - 0.74\ln\left(1+y_{cw}\right) \qquad (16)$$

where the combined wave/current orbital diameter designated d_{cw} is

$$d_{wc} = \left(d_w^2 + \left(T\overline{u_d}\right)^2 + 2d_w\left(T\overline{u_d}\right)\cos q\right)^{0.5} \qquad (17)$$

with θ representing the angle between waves and currents, $\overline{u_d}$ = the current velocity at the top of the boundary layer, and T = the wave period, and the combined flow mobility number

$$y_{cw} = \frac{U_{cw}^{\ 2}}{(s-1)gD} \tag{18}$$

is the ratio of the combined flow velocity (U_{cw}) squared to the immersed weight per unit area of the bed according to

$$U_{cw} = \left(\frac{U_d}{p}\right)2 + \bar{\bar{u}}^2 + 2\frac{U_d}{p}\bar{\bar{u}}\left|\cos q\right| \tag{19}$$

with the depth-averaged current velocity $\bar{\bar{u}}$ replacing $\overline{u_d}$ from (17).

Khelifa and Ouellet's [2000] ripple height formula is expressed as

$$\frac{2h}{d_{cw}} = 0.32 + 0.017\ln^2(1+y_{cw}) - 0.142\ln(1+y_{cw}) \tag{20}$$

Similarly, *Li and Amos* [1998] applied wave-dominated ripple prediction equations to their field data and concluded that wave-ripple predictors significantly over-predict ripple height and roughness for combined flows. *Li and Amos* [1998] classified combined-flow ripples into three categories based on the ratio of skin friction wave shear (u_{ws}) to skin friction current shear velocity (u_{cs}): wave dominant ($u_{ws}/u_{cs} > 1.25$), current dominant ($u_{ws}/u_{cs} < 0.75$), and combined wave-current ripples ($0.75 < u_{ws}/u_{cs} < 1.25$). Their proposed ripple height predictors for both wave dominant and combined flow produced ripples are as follows.

For wave dominant ripples,

$$\frac{h}{D} = 27.14\left(\frac{u_{cwb}}{u_{cr}}\right) + 16.36 \qquad (21)$$

where u_{cwb} is the bedload shear velocity and u_{cr} is the critical shear velocity for bedload transport. The wave-current ripples were modeled according to

$$\frac{h}{D} = 22.15\left(\frac{u_{cwb}}{u_{cr}}\right) + 6.38 \qquad (22)$$

In addition to waves and mean currents, other oceanic phenomena such as bound long waves affect sediment transport. Bound long waves are within the infragravity frequency range (f < 0.05 Hz, or T > 20s), and serve as a restoring force for the variation in short wave momentum of incident wave groups. As a wave train consisting of wave groups (surf beat) and the associated bound long waves begin to shoal, the waves become non-linear with peaked asymmetric crests and long, flat troughs [*Longuet-Higgins and Stewart*, 1962]. The waves' positively skewed orbital velocity suspends and transports sediment onshore, while the lower frequency currents transport suspended sediment either onshore, offshore, of alongshore depending on the current's mean direction. The bound long waves under wave groups, however, provide a net offshore transport. Both *Shi and Larsen* [1984] and *Deigaard et al.* [1999] conclude that because bound long waves produce an offshore flow under high waves in the group when the suspended sediment concentrations are high, and an onshore flow under the low waves with low suspended sediment concentrations, a net offshore sediment transport results. An investigation of the relative importance of these different transport mechanisms derived from laboratory and field studies would greatly aid in predicting net sediment transport [*Deigaard et al.*, 1999].

To gain a better understanding of sediment transport and ripple geometry, several methods of observing ripple structure and migration have been utilized in the field. Many previous field studies have relied upon crude in situ observations conducted by

divers, which greatly limits temporal and spatial sampling of bottom bedforms. *Boyd et al.* [1988], *Amos et al.* [1988], and *Wheatcroft* [1994] used photographic measurement time-series to characterize ripple wavelength, orientation, and migration rates under varying oceanographic conditions. *Li and Amos* [1998] also used photographic equipment to monitor the bed, but included a shadow bar to aid in determining ripple height. These optical methods for two-dimensional bedform monitoring lack accuracy, and perform poorly during periods of high suspended sediment concentration.

Hay and Wilson [1994] and *Traykovski et al.* [1999] employed rotary sidescan sonar systems to quantify bedform evolution in their nearshore field studies. High resolution images of bedform development were obtained in this manner, and ripple wavelength and migration rates were determined. Similar to the photographic systems, however, this apparatus is limited by its inability to ascertain bedform amplitudes.

The Monterey Inner Shelf Observatory (MISO) was designed and implemented by *Stanton* [1999] to obtain continuous observations of bedforms in 12m of water while simultaneously monitoring wave and current conditions. A scanning acoustic altimeter and an acoustic Doppler current profiler obtained high resolution measurements of ripple geometry and flow, respectively. The objective of this paper is to analyze the wave, current, and bedform response data collected by MISO off the coast of Monterey, California during the year 2000. Due to the length of the time-series, the data spans a wide range of dynamic oceanic conditions and various bed responses, spanning relict, active ripple formation, and sheet flow conditions. Existing ripple models are evaluated using these field data.

THIS PAGE INTENTIONALLY LEFT BLANK

II. SITE DESCRIPTION

The Monterey Inner Shelf Observatory (MISO) is part of an on-going program focused on littoral oceanographic observation and modeling at the Naval Postgraduate School, Monterey, CA. MISO, a component of the Rapid Environmental Assessment Laboratory (REAL), consists of an underwater frame supporting five instruments. It is located in 12m of water 600 m off the Del Monte Beach at the southern end of the Monterey Bay (Lat. 36° 36.29' N; Long. 121° 052.53' W; Figure 1) on a broad, sandy channel between shale beds to the north and south. The frame is mounted over a mobile bed of well-sorted quartz sand with a 0.260 mm median grain diameter (d_{50}) (Figure 2). Waves incident on the MISO location tend to be narrow-banded from the northwest due to the strong refractive effects of the Monterey Bay Canyon as well as the protection provided by the Point Pinos and Santa Cruz headlands (Figure 1).

MISO is connected to a shore terminus by a fiber optic data and power cable. A meteorological station in the sand dunes inshore augments the data collected underwater by measuring 10m height wind speed and direction, air temperature and dew point, short and long wave incident radiation, barometric pressure, and rain fall rates. Figure 3 illustrates the MISO and meteorological station's configuration.

MISO began collecting data on July 26, 1999, and the meteorological station began on April 28, 2000. Although the data set is not complete (due to routine maintenance and instrument removal/repair), a large portion of continuously sampled data is available for study. This study focuses exclusively on the year 2000 data as it contains the most continuous time-series of velocity and bedform measurements (Figure 4). This time period provides comprehensive data spanning energetic winter to relatively quiescent summer conditions. The average significant wave height for this time-series is 0.5 m with a peak around 2 m.

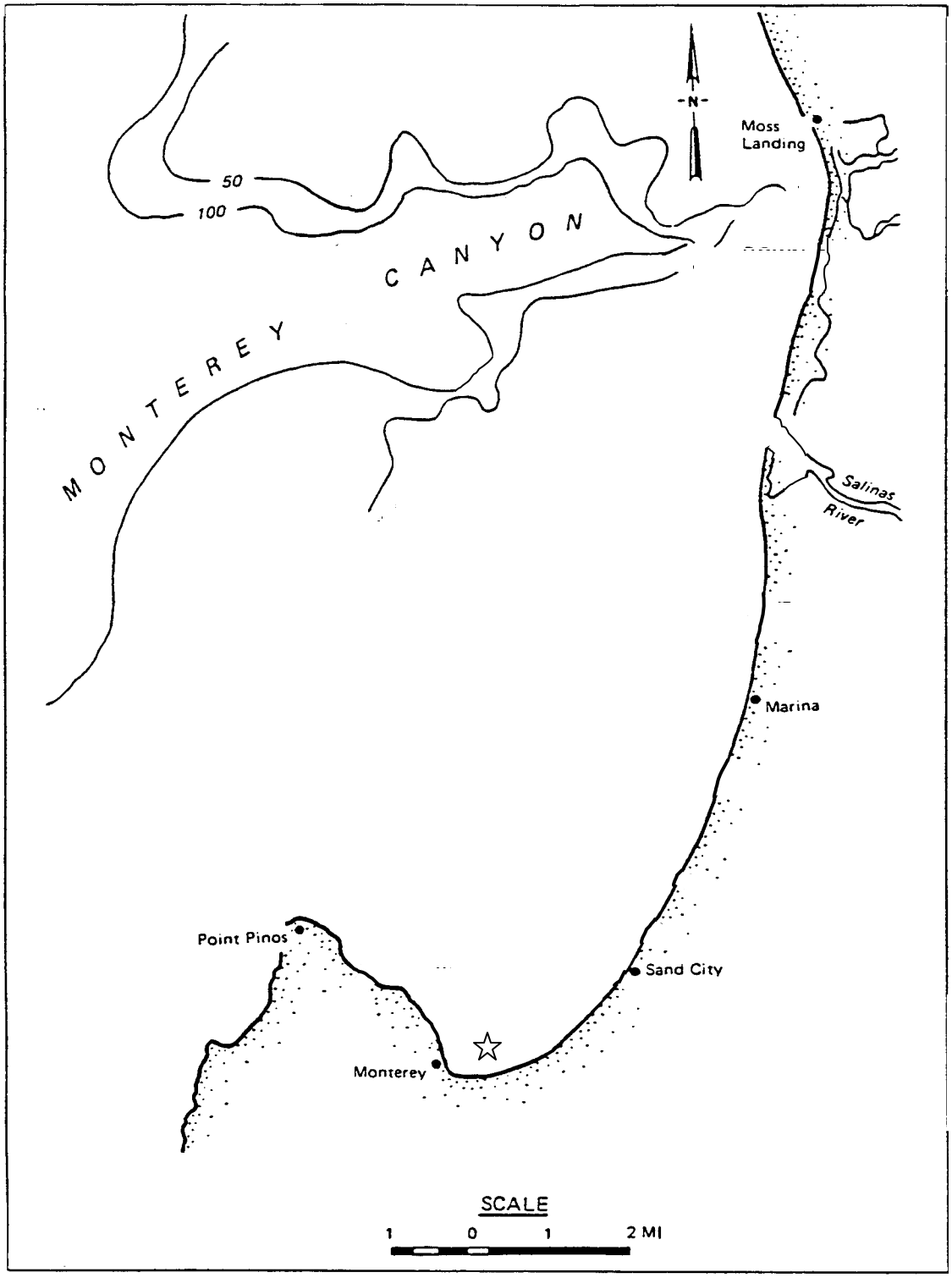

Figure 1. Location of the MISO instrument platform off Monterey, CA. The star represents the location of the MISO array.

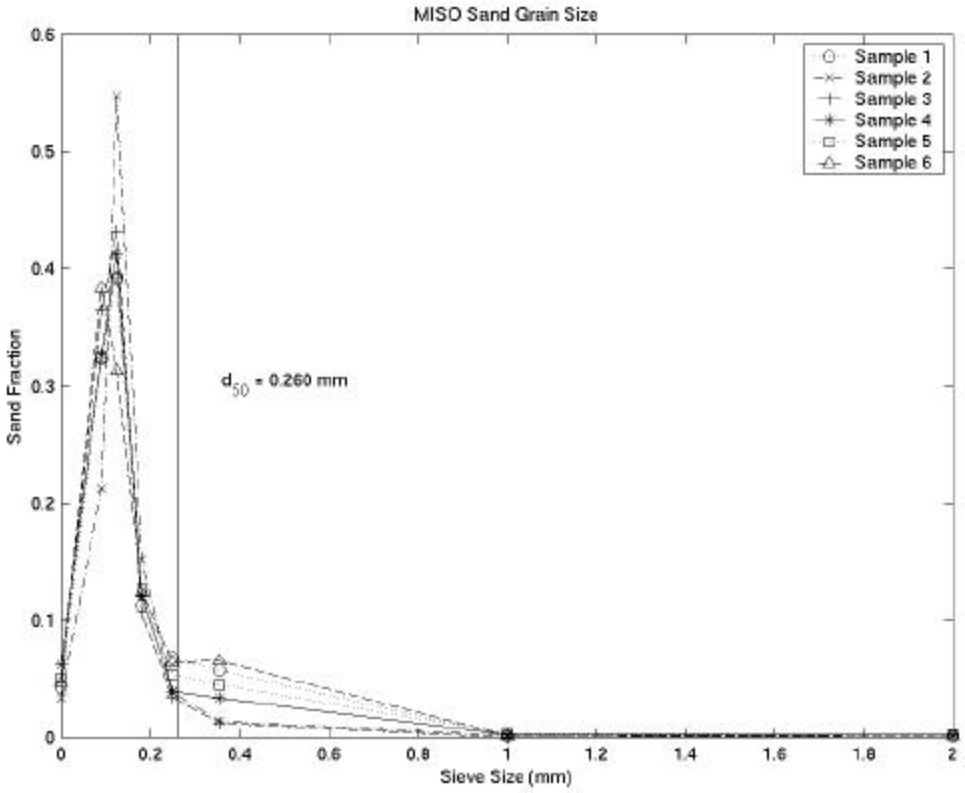

Figure 2. Sand grain size distribution of six sand samples taken at the MISO site. The median grain size (d_{50}) of these samples is 0.260 mm.

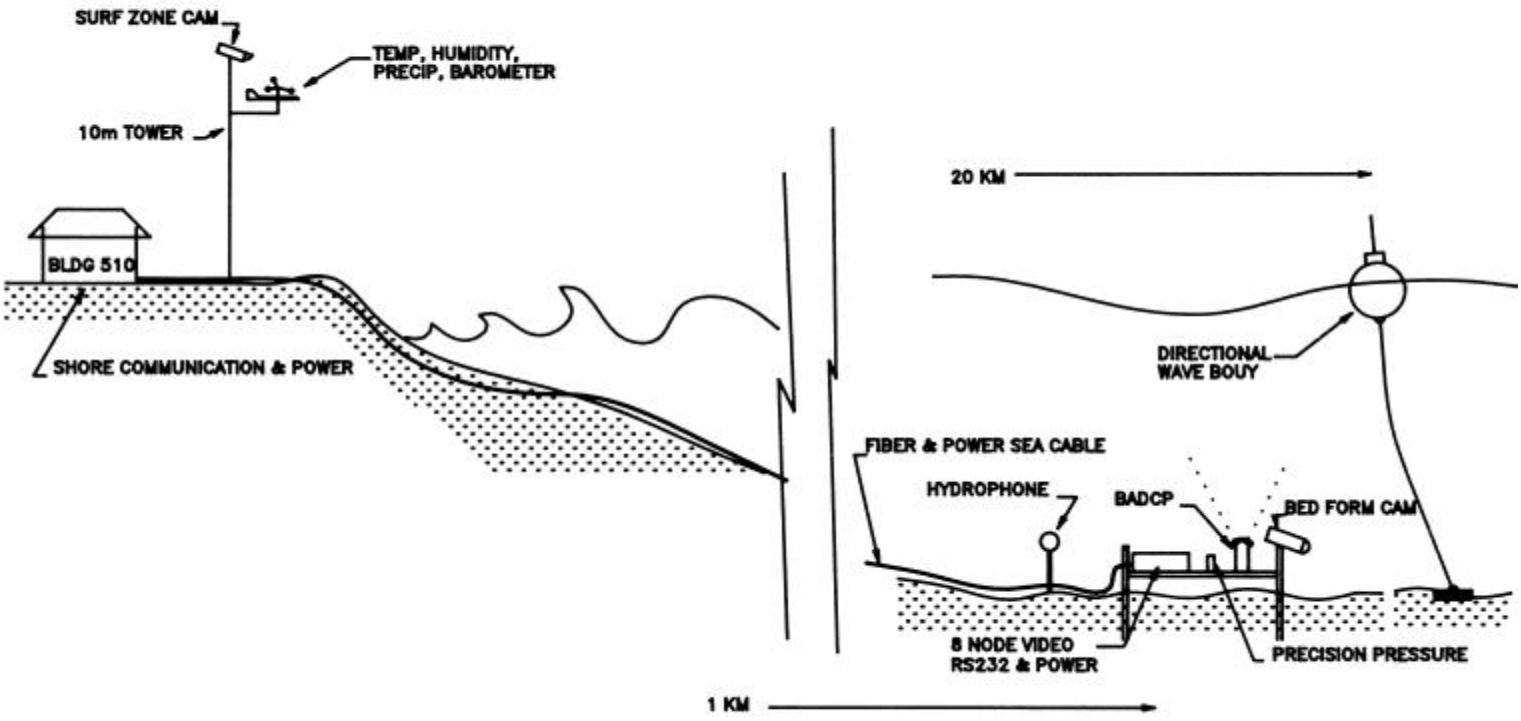

Figure 3. MISO frame and meteorological station configuration [*Stanton*, 1999].

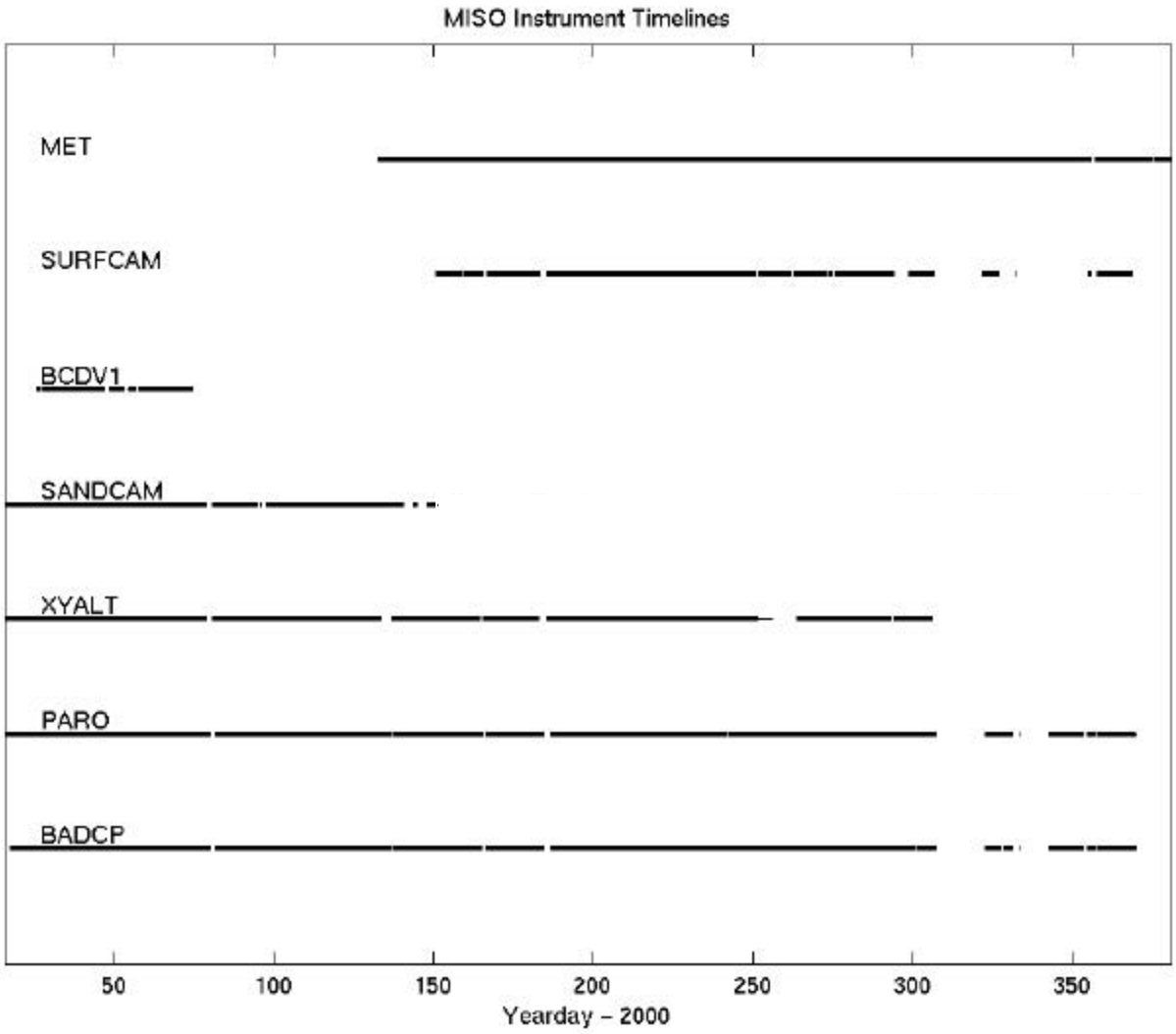

Figure 4. MISO instrument timeline for the year 2000. The above timeline indicates when each instrument mounted on the MISO frame and meteorological tower collected data. Gaps indicate instrument maintenance periods. [MET – meteorological station instruments; SURFCAM – surf camera mounted on the meteorological station; BCDV1 – Bistatic Coherent Doppler Velocity and Sediment Profiler; SANDCAM - Structured Light and Camera; XYALT – Scanning Acoustic Altimeter (SAA); PARO – Paro-Scientific pressure sensor; BADCP – Bottom Acoustic Doppler Current Profiler]

THIS PAGE INTENTIONALLY LEFT BLANK

III. INSTRUMENTATION AND DATA PROCESSING

The MISO frame mounts five instruments for monitoring bedforms and wave and current forcing: a Broadband Acoustic Doppler Current Profiler (BADCP), Paro-scientific pressure sensor, Scanning Acoustic Altimeter (SAA), Structured Light and Camera (SLAC), and a Bistatic Coherent Doppler Velocity and Sediment Profiler (BCDVSP). Figure 5 illustrates the placement of these instruments on the MISO frame. The BADCP measures the current velocities every 1m from the frame to the near ocean surface, allowing mean currents and characteristics of surface waves to be determined. The Paro-scientific pressure sensor measures the height of water above the frame to produce a record of tides and long period waves. The SAA continuously maps the sandy bed offshore of the MISO frame, producing a time-series of the changing bedform conditions for a 1m alongshore by 1.5m cross-shore area, while the SLAC produces photographic images of a 1m by 1m area to quantify small-scale bedforms. The BCDVSP measures the velocity and sediment concentration above the bed. These small-scale measurements are used to define the mean and turbulent structure of the water column above the bed resulting from combined flow conditions over the evolving bedforms. This study utilizes data from the BADCP and SAA as they provide the most continuous velocity and ripple measurements, respectively (Figure 4), for a year-long period.

A. BROADBAND ACOUSTIC DOPPLER CURRENT PROFILER (BADCP)

1. Data Acquisition

An RDI Instruments' Broadband Acoustic Doppler Current Profiler (BADCP) measured horizontal current velocities at the MISO site by transmitting broadband pulses of 1.2 MHz frequency sound waves along each of four narrow acoustic beams, slanted 20 degrees from the vertical. Each transducer then measured the echoes returned from sound scatterers (small particles or plankton) suspended in the water column at 1m range intervals up to the sea surface. As the mean currents carried the sound scatterers to or from the ADCP, the sound waves at the scatterers' location become Doppler-shifted to

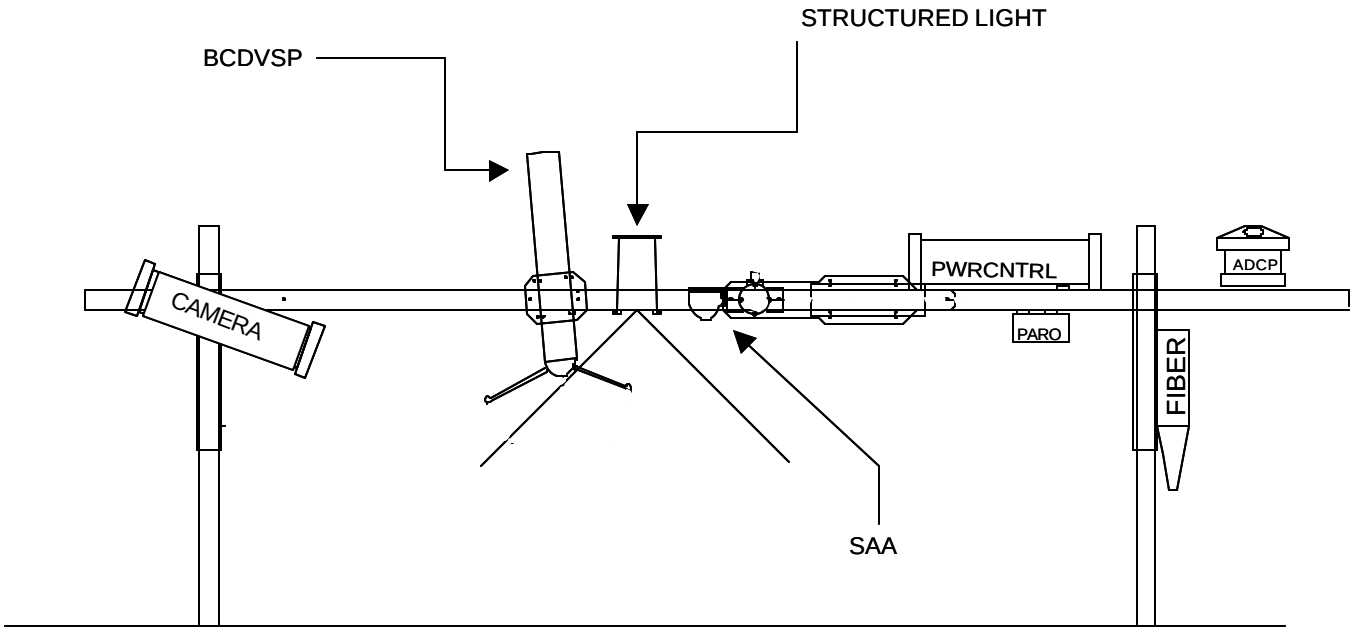

Figure 5. MISO instrument frame as viewed from offshore looking inshore. The instruments include (from left to right): camera component of the Structured Light and Camera (SLAC), Bistatic Coherent Doppler Velocity and Sediment Profiler (BCDVSP), structured light component of the SLAC, Scanning Acoustic Altimeter (SAA), Paro-scientific pressure sensor, and the Broadband Acoustic Doppler Current Profiler (BADCP).

higher or lower frequencies. This Doppler-shift is proportional to the relative velocity between the ADCP and the scattering particles. By measuring Doppler shifts with a four-beam configuration, the ADCP resolved horizontal current velocities into 1m range-averaged depth cells, or bins, at a sampling frequency of 0.976 Hz. A high resolution strain gage pressure transducer in the BADCP head measured the water pressure at the same sample frequency.

The horizontal velocities measured at the MISO site were oriented relative to the ADCP instrument and MISO frame at a magnetic heading of 313° M. Following an error-removal process, the current velocity measurements were remapped into a cross-shore normal coordinate system. The velocity vectors were rotated 7° + 90° such that the

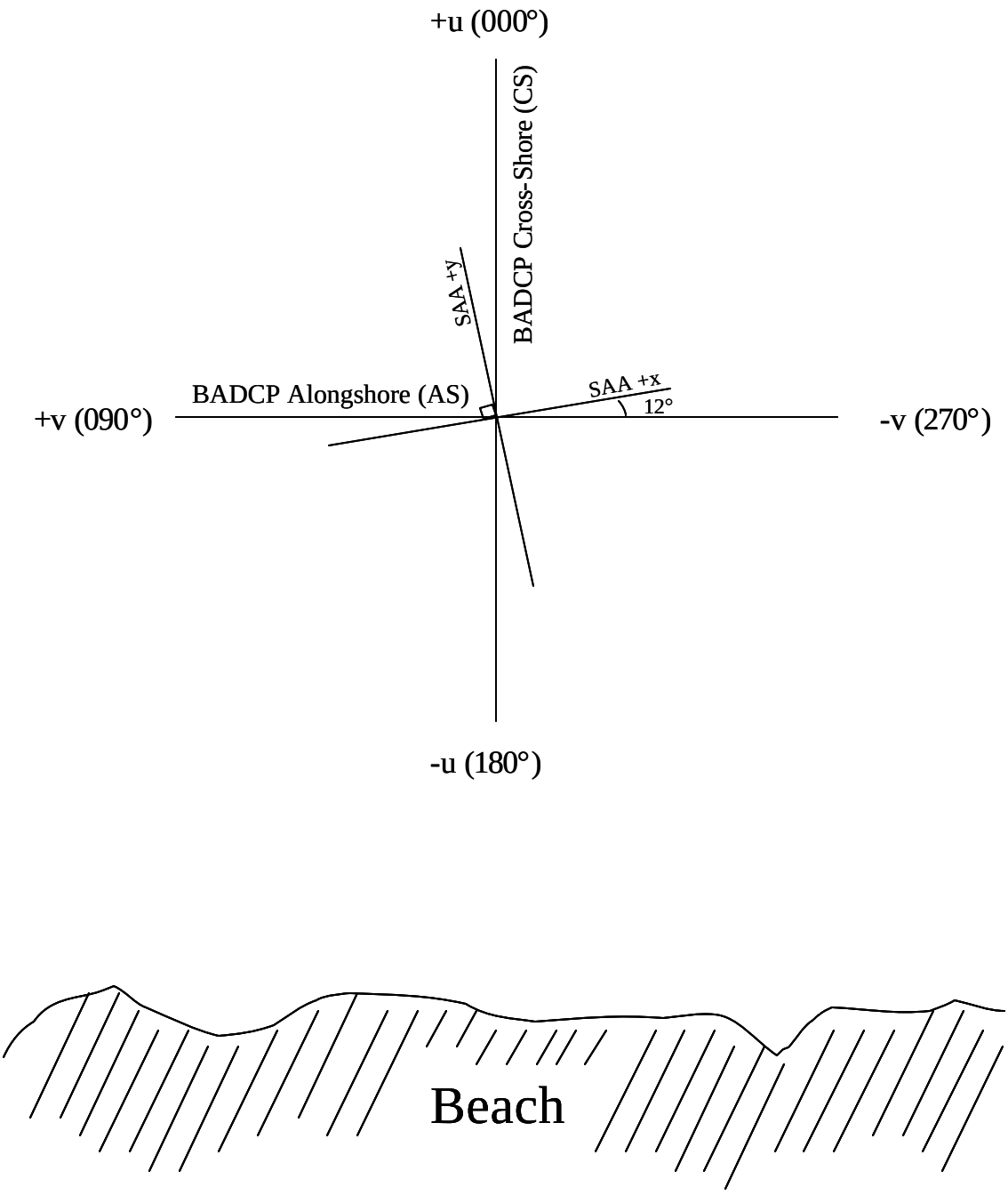

Figure 6. Cross-shore normal coordinate system for horizontal current velocities measured by the Bottom Acoustic Doppler Current Profiler (ADCP) as well as the orientation for the Scanned Acoustic Altimeter (SAA) at the MISO site off Del Monte Beach, Monterey, CA.

+*u* vector corresponded to the nominal cross-shore (CS) direction and the +*v* vector corresponded to the alongshore (AS) direction as shown in Figure 6.

The raw ADCP data time series was segmented into one-hour ensembles for statistical analysis to provide stable estimates of dynamic forcing variables at the site. The first 1m bin of the ADCP vertical profile was discarded due to velocity errors induced by the water's interaction with MISO's equipment frame. The second velocity bin (~2m off the bottom, or $z \approx 10$m) was utilized to characterize the near-bed velocity field well outside of the thin, oscillatory boundary layer. The linear wave transfer functions for swell waves typical of the site are presented in Figure 7. The near-bed depths of 12m produced transfer function values within 5% of those at 10m depth for typical wave periods of 8, 10, and 15s. For this reason, the 10m velocity measurements were used to represent the near-bed velocities just outside the thin oscillatory boundary layer above the bed.

2. Error Removal Procedure

A concern in processing the multiyear ADCP time-series from the MISO experiment was distinguishing the true current velocities near the bed from occasional erroneous values. Even infrequent spurious velocity estimates had to be removed to ensure meaningful high-order statistics. Errors not representative of true current velocities likely occurred in the broadband ADCP data as a result of fish or seaweed passing in front of the transducers, which in turn generated poor beam correlation values. These intermittent errors could be seen upon visual inspection of the raw time-series plots of alongshore (AS) and cross-shore (CS) current velocity measurements. Error detection and removal using an interactive editor, however, would have been tedious and time consuming. Instead, these erroneous data points were identified and removed in an automated error removal routine utilizing four discriminating steps: (1) a correlation level test, (2) a normalized difference test, (3) a temporal difference test, and (4) an outlier value test. All current velocity data were deglitched in hourly sections prior to further analysis using the following criteria.

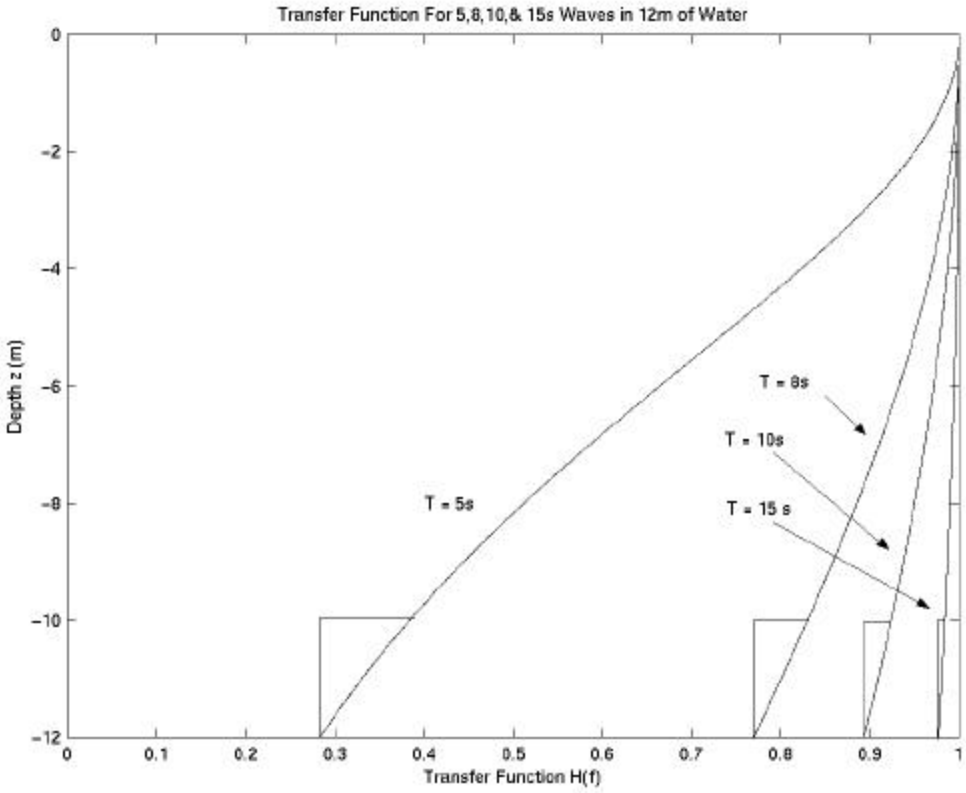

	T = 5s	T = 8s	T = 10s	T = 15s
z = 10	0.3839	0.8301	0.9240	0.9842
z = 12	0.2833	0.7698	0.8935	0.9774

Figure 7. Vertical profile of linear wave theory transfer function for ADCP velocity measurements of 5, 8, 10, and 15s period waves in 12m of water. The transfer function $H_b(f) = \frac{1}{\cosh(k(h+z))}$, where k is the wavenumber and h+z is the distance above the bed, produced roughly equivalent values for 10m and 12m depth velocity measurements.

a. Step 1: ADCP Correlation Level Test

In addition to ascertaining the along-beam current velocity at a given time and given range bin, the ADCP also recorded the data quality returned in the form of a correlation value. The correlation magnitude measured the normalized echo autocorrelation at the lag used for estimating the Doppler phase change of each beam (RDI, 1998). The Workhorse ADCP represented correlation values in a linear scale between 0 and 255, with 255 being a perfect correlation (i.e. a solid target with no system or acoustic noise), and 0 indicating the poorest correlation. Low correlation values in the MISO ADCP data may have been caused by low scattering particle concentrations or near-field objects obscuring the transducer, resulting in poor signal-to-noise ratios. To remove erroneous velocity estimates resulting from poor correlation magnitudes, all four beams' correlation values were first added together at each time and range bin. Upon determining the mean and standard deviation of the summed correlation values over a one-hour interval, a threshold was established:

$$C_{thr} = C_{mean} - CorrC * C_{rms} \tag{23}$$

where C represents the correlation time-series, and *CorrC* is a constant pre-selected value (see Table 1). If the correlation values dropped below this threshold at any point in the one-hour time-series, the velocity data was flagged as erroneous, and removed from the data set. This method provided adaptive criteria for rejecting velocity estimates using the correlation time-series, which could vary slowly as backscatter and fluid flow conditions changed through the yearlong time-series.

b. Step 2: Normalized Range Bin Difference Test

A clear indication of errors or spikes in the data was observed when the time-series of two adjacent velocity bins were compared. While it was expected that the velocity measurements between each bin would vary at any given time, the along-beam difference velocities are bounded for a given wave height above the bed and mean current shear. Large differences in velocity from one bin to another near the bed might indicate the presence of fish or other anomalous scattering particles. In order to detect significant vertical differences of horizontal current velocity, the difference between two bins' velocity vectors was normalized by their standard deviation. If the normalized difference between the bins at each sample point was greater than *NormC*, the velocity data was rejected:

$$U_{thr} = \left| \frac{U_{difference}}{U_{rms}} \right| > NormC \qquad (24)$$

where $U_{difference} = U_{bin2} - U_{bin3}$, U_{rms} is calculated over each one-hour interval, and *NormC* is a predetermined threshold value. U_{thr} provided a conservative threshold that adapted to the average wave forcing over each hour.

c. Step 3: Temporal Difference Test

The third procedure in the deglitching sequence removed errors/spikes not identified in the correlation or normalized difference correction methods by testing the fluid acceleration between successive samples. First differences in time were calculated for the velocity time-series, and values exceeding the threshold $\pm DespC * \sigma$ and not extending for more than 4 sample intervals (≈4 seconds) were replaced with interpolated values using a linear interpolation scheme. The objective of this criterion was to remove large slew, single point outliers from the time-series.

d. Step 4: Outlier Value Test

As a final precaution, all remaining outlying data points were removed by first demeaning the velocity data set. All demeaned velocity data points whose absolute value was greater than the large pre-selected threshold value *OutC* * σ were removed and replaced with flagged error values:

$$O_{thr} = \left| U_{demeaned} \right| > OutC * U_{rms} \tag{25}$$

Once all of the errors were identified and replaced with flagged values, a gap replacement routine filled gaps < 5 time intervals (≈5 seconds) in length with the mean current velocity. Thus, small gaps resulting from errors induced by low correlation values or spurious scattering particles in the water column would not affect subsequent statistical measurements. Larger gaps, however, remained after the replacement process and posed a problem in higher-order statistical computations. For this reason, high-order statistical quantities were only derived from continuous data segments greater than twenty minutes in length.

e. Statistical Analysis of the Error Removal Procedure

Great care was taken to make the data set as self-consistent as possible by establishing conservative threshold levels that would not reject valid, large amplitude data points in the velocity time-series. The alongshore current (AS) velocity time-series of yeardays 2000078 (MAR 2000) and 2000137 (MAY 2000) are used as examples to illustrate the removal of erroneous velocity samples and the choice of threshold values. Figure 8 shows that day 078 was highly energetic with AS velocities 2m above the bed

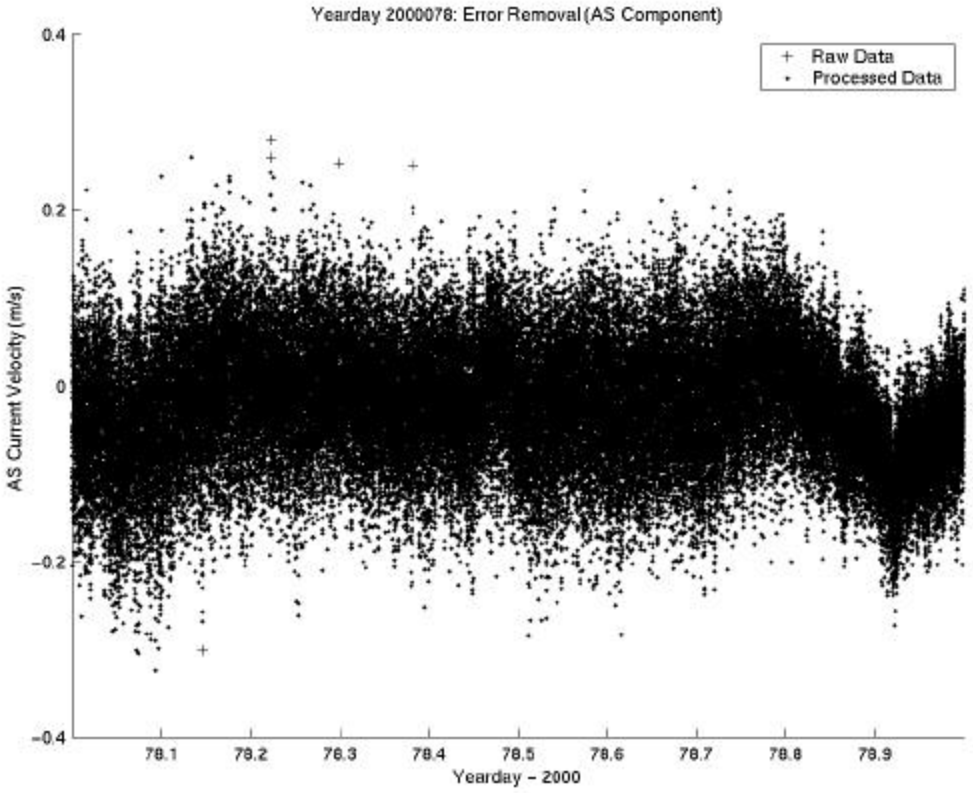

Figure 8. Alongshore (AS) raw and processed ADCP velocity data time-series for high-energy yearday 2000078.

oscillating between –0.2 and 0.2 m/s, while Figure 9 shows that day 137 was calmer as evidenced by lower velocity magnitudes ranging from –0.1 to 0.1 m/s at the same depth. The corresponding cross-shore component magnitudes (not pictured) ranged from –0.8 to 0.8 m/s and –0.2 to 0.2 m/s for yeardays 078 and 137, respectively. The processed data in both figures is a result of applying conservative threshold levels to the raw ADCP velocity data at each stage of the error removal process. Table 1 provides a summary of the various threshold categories tested for each step of the error removal process, and indicates the selected threshold levels used to obtain the processed data in these figures.

To measure the effectiveness of the error removal sequence, kurtosis coefficients were calculated for various threshold levels at each hour time interval. The kurtosis coefficient, or 4^{th} central moment divided by the fourth power of the standard deviation, is a measure of distribution peakedness, and is highly sensitive to erroneous

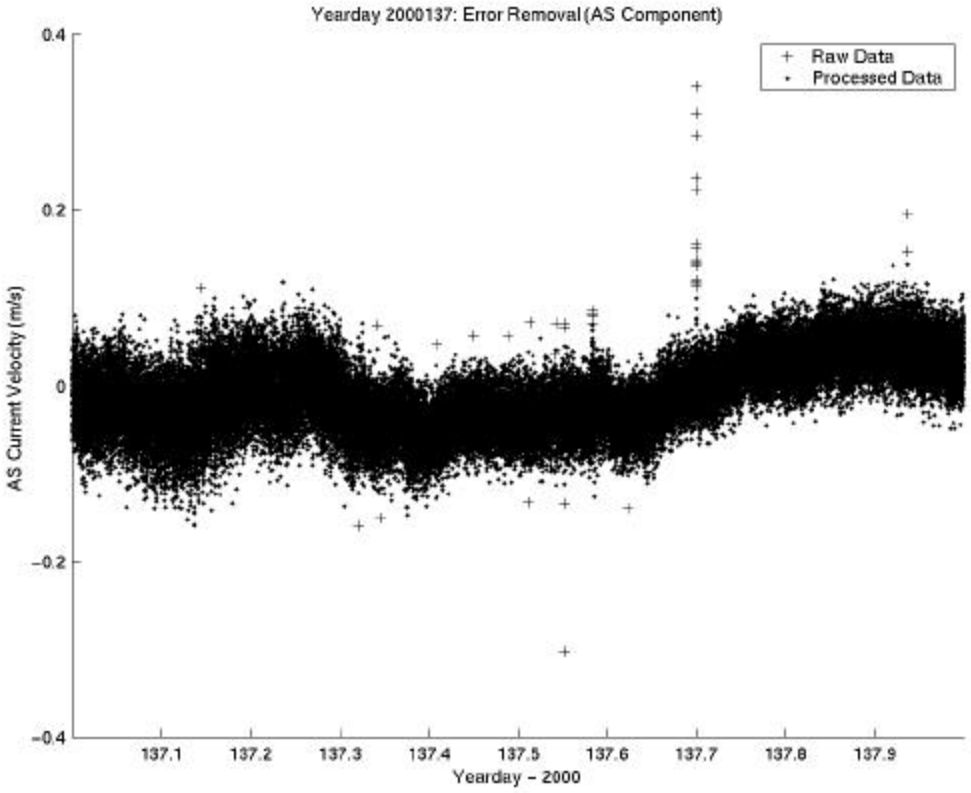

Figure 9. Alongshore (AS) raw and processed ADCP velocity data time-series for low-energy yearday 2000137.

Table 1. Error removal threshold names and values. Selected threshold values correspond to the levels used in the error removal process, while low and high values are used to validate those selections.

Threshold Correction Name	Threshold Abbreviation	Low Threshold Values	Selected Threshold Values	High Threshold Values
Correlation	CorrC	3	4	5
Normalized Range-Bin Difference	NormC	4	5	6
Temporal Difference Despike	DespC	3	4	5
Outlier	OutC	3	4	5

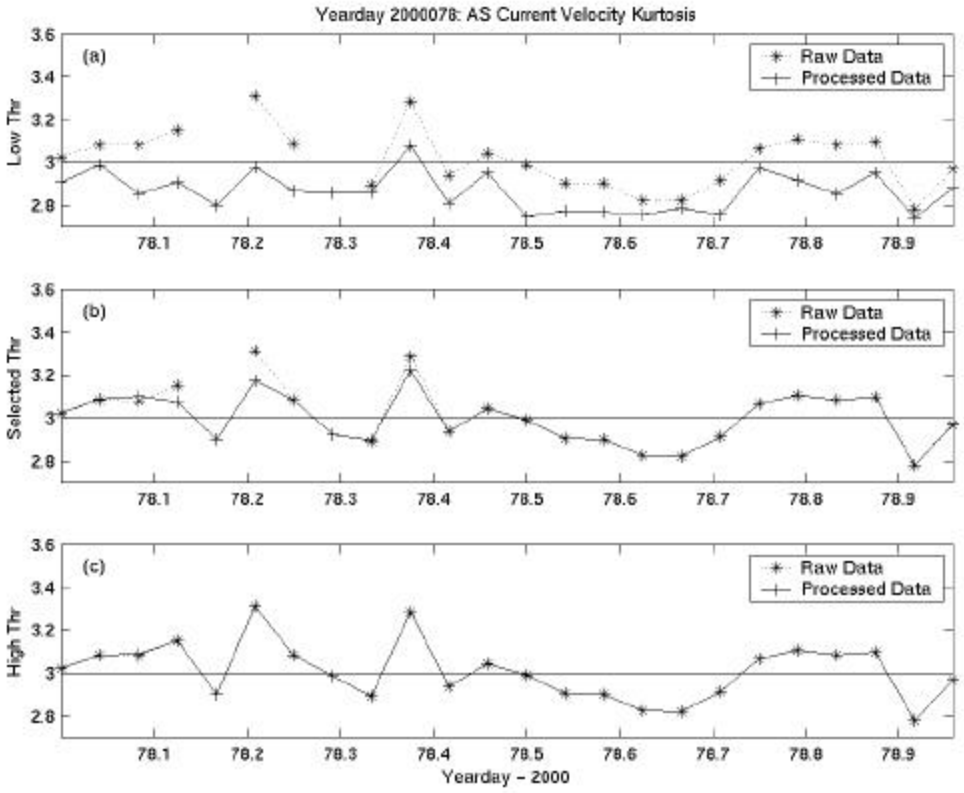

Figure 10. Hourly kurtosis coefficients for alongshore (AS) ADCP velocity data time-series for yearday 2000078: (a) using low threshold values, (b) using the selected threshold values, and (c) using high threshold values.

outlying data points. For this reason, it was used to determine the robustness of the error removal process. A kurtosis value of 3 would indicate that the velocity distribution was normal, while values greater than 3 would indicate outlying data points. If the kurtosis values dropped below 3, the data distribution became flatter than normal, indicating too many data points had been removed from the time-series. The automated data editing algorithm required that true changes in high order statistics be retained while occasional erroneous values are removed. Figures 10 and 11 show the AS hourly kurtosis values for each example yearday with different threshold categories: low, selected, and high.

Thresholds were systematically chosen for each deglitching criterion by observing the number of data points being removed or replaced as well as the data distribution's peakedness response to various correction levels. The threshold levels that were conservatively selected are as follows: correlation correction (*CorrC*) = 4,

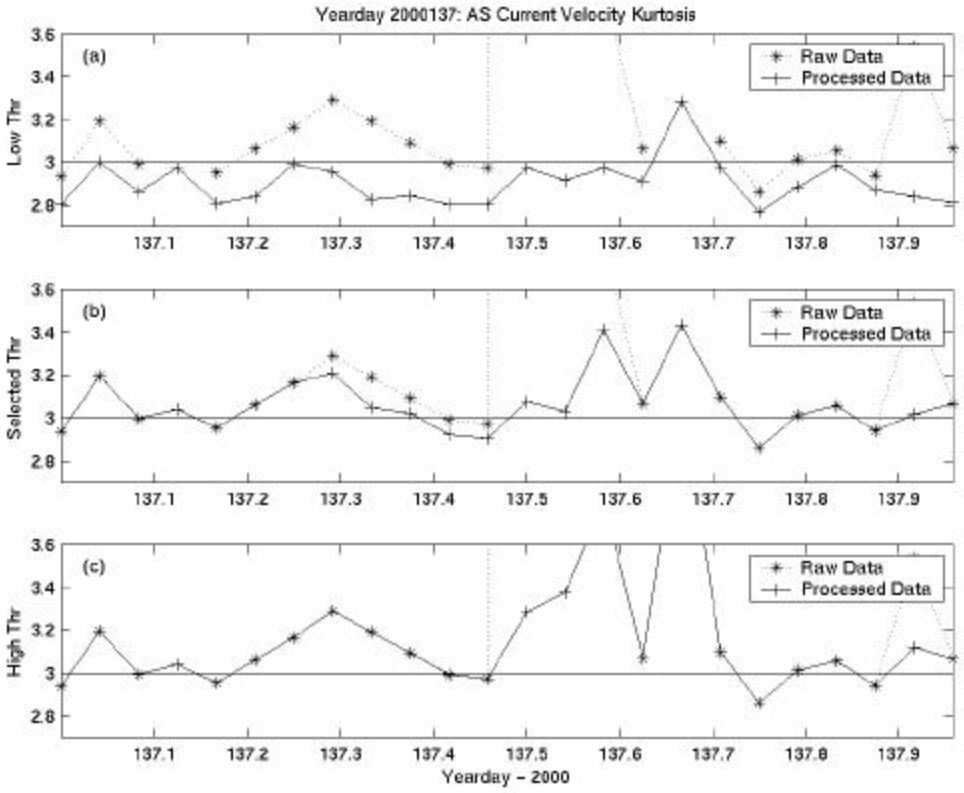

Figure 11. Hourly kurtosis coefficients for alongshore (AS) ADCP velocity data time-series for yearday 2000137: (a) using low threshold values, (b) using the selected threshold values, and (c) using high threshold values.

normalized range bin difference correction (*NormC*) = 5, temporal difference despike correction (*DespC*) = 4, and outlier correction (*OutC*) = 4. Figures 12 and 13 illustrate how many data points were removed / replaced according to each step with the selected threshold levels for both yeardays. The number of corrected data points for each criterion as well as the total number of data points is contained in Table 2. The results of lowering the threshold values (i.e. removing more data points by decreasing each selected level by 1) as well as the number of data points removed / replaced in accordance to high threshold levels (i.e. retaining more data points by increasing each selected level by 1) are also displayed in Table 2 and plotted in Figures 12 and 13.

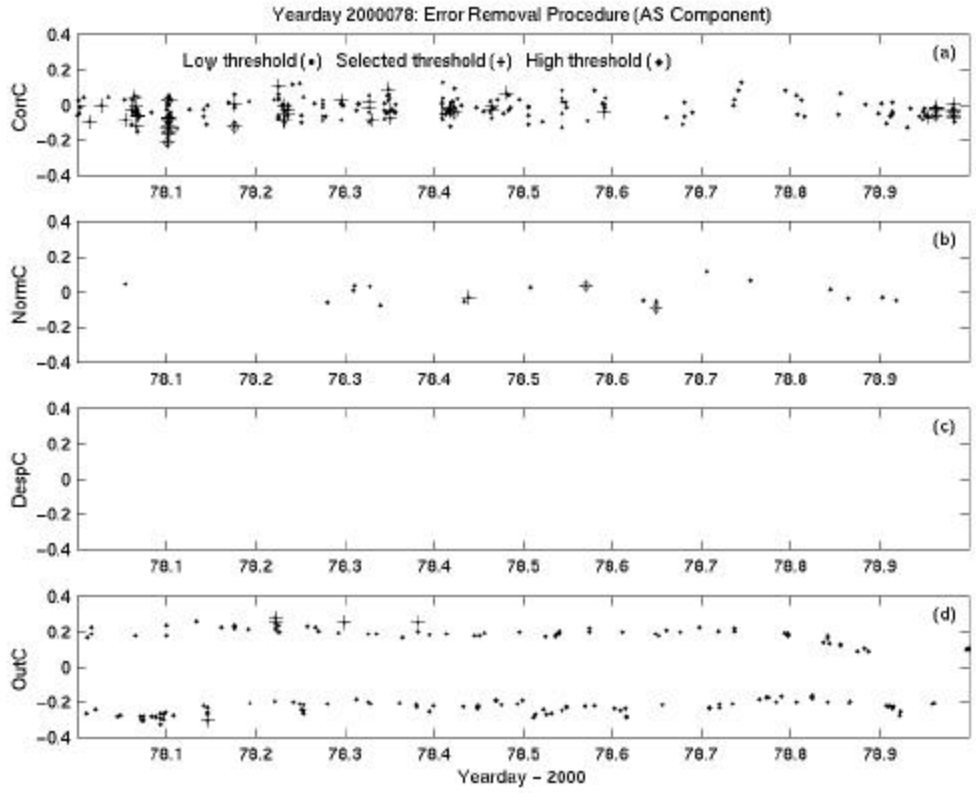

Figure 12. Data points flagged as errors for the alongshore (AS) ADCP velocity data on yearday 2000078 according to each step of the error removal procedure: (a) correlation correction, (b) normalized range bin difference correction, (c) temporal difference despike correction, and (d) outlier correction for low, selected, and high threshold values.

One consequence of lowering each threshold value to *CorrC* = 3, *NormC* = 4, *DespC* = 3, and *OutC* = 3 was a significant reduction in kurtosis values due to the removal of too many data points (Figures 10(a) and 11(a)). For energetic days, reducing the correlation correction from 4 to 3 increased the number of data points removed by a factor of 5-10, while reducing the temporal difference and outlier correction levels produced similar results. For low-energy days, a reduction in the correlation correction threshold was not as significant. Reducing the temporal difference and outlier correction thresholds, however, increased the number of data points rejected ten-fold in low-energy days. Figures 12 and 13 both show too many data points being identified as erroneous in the low threshold time-series. This conclusion is validated upon inspection of the

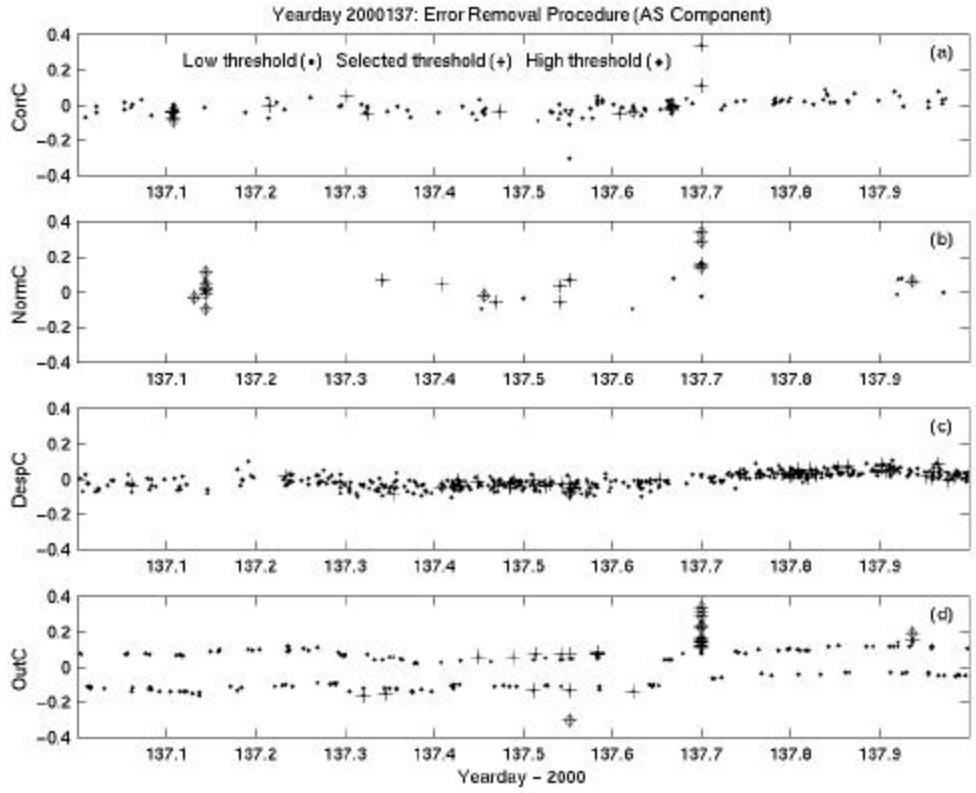

Figure 13. Data points flagged as errors for the alongshore (AS) ADCP velocity data on yearday 2000137 according to each step of the error removal procedure: (a) correlation correction, (b) normalized range bin difference correction, (c) temporal difference despike correction, and (d) outlier correction for low, selected, and high threshold values.

corresponding kurtosis calculations. All low threshold values produced current velocity kurtosis values lower than the normal distribution value of 3. Clearly, removing too many data points resulted in a significantly altered velocity distribution.

Increasing the threshold values to *CorrC* = 5, *NormC* = 6, *DespC* = 5, and *OutC* = 5, on the other hand, proved to retain too many erroneous outlying data points (particularly during the low-energy days such as day 137). While the goal in removing errors from the data set was to retain as much of the large amplitude data points as possible, these high thresholds were retaining many outlying data points and producing

Table 2. Number of erroneous data points for the alongshore ADCP velocity data on yearday 2000078 and 2000137 according to each step of the error removal procedure using different threshold level categories.

Day 078		Low	Selected	High	Total Nuber of
	CorrC	257	53	8	Data Points
	NormC	19	3	2	67077
	DespC	0	0	0	
	OutC	173	5	0	
	Total	449	61	10	
Day 137		Low	Selected	High	Total Nuber of
	CorrC	141	16	3	Data Points
	NormC	36	21	12	67311
	DespC	486	44	3	
	OutC	218	33	13	
	Total	881	114	31	

data distributions with high kurtosis values close to those of the raw data distributions (Figures 10(c) and 11(c)).

For these reasons, the selected threshold values were established at *CorrC* = 4, *NormC* = 5, *DespC* = 4, and *OutC* = 4. Of particular interest was the fact that the high-energy days contained more correlation corrections than the low-energy days. The numbers of normalized-difference, temporal difference, and outlier corrections, however, were more frequent during low-energy days. The high-energy days contained raw velocity data kurtosis values close to 3, while the low-energy days had very large, erratic kurtosis peaks resulting from data errors in the raw data distribution. Both of these observations are reasonable. Very energetic days with swift oscillatory currents generated low correlation values due to high fluid speeds through the sample volumes, and contained relatively few outlying data points. (Fish are less likely to be grazing near the bed during high currents.) In contrast, low-energy days with weak current velocities reduced the possibility for low correlation values by making occasional detections of fish more noticeable. Any scattering particles in the water column had a higher residence time in the ADCP's beam path than during very energetic conditions. This would account for the increase in outlying data points and the consequent peaks in kurtosis values obtained during low-energy time periods.

To better demonstrate the effectiveness of the selected thresholds, Figure 14 presents the error-removal sequence for one hour of yearday 2000176 velocity data where there were large spikes in kurtosis values for the raw, unprocessed data. The need for these four largely independent criteria is also illustrated. On yearday 2000176, hour 13, the kurtosis coefficient for the AS velocity component was ≈ 16.7. Figure 14(a) shows the time-series for this hour. Three peaks (one negative, two positive) of outlying data points in the raw data clearly show why the kurtosis coefficient was high. Both the correlation correction (Figure 14(b)) and the normalized range bin difference correction (Figure 14(c)) removed two errors using the selected threshold values. The despiking routine and the outlier correction both resolved the outliers near 176.565 by removing and interpolating across the spike using a selected threshold value of 4σ (Figure 14(d)). The resulting kurtosis coefficient from the error removal sequence is ≈ 3.00. The deglitching sequence returned the AS velocity distribution of that hour to normal while removing and replacing only 29 / 2796 data points (1.04%). If that same hour of data was deglitched according to low threshold values, 50 / 2796 (1.79%) of the data would be rejected and corrected producing a kurtosis value of 2.88. High threshold standards would remove only 21 / 2796 (1.07%) of the data, yielding a kurtosis coefficient of 3.13. The selected threshold values produced the best data distribution with minimal corrections for the yearlong time-series for twelve audit cases chosen from the yearlong time-series.

3. Statistical Analysis

Forcing of the bed was characterized by calculating statistics of the 2m level current time-series for each one-hour interval through the year 2000. The mean and the RMS velocities were the only quantities calculated on the raw data time-series. The RMS velocity time-series provided a good indication of energetic wave forcing yeardays. The higher order statistics skewness and kurtosis were calculated from the error-removed gapless time-series. The skewness coefficient is a measure of the degree of asymmetry of

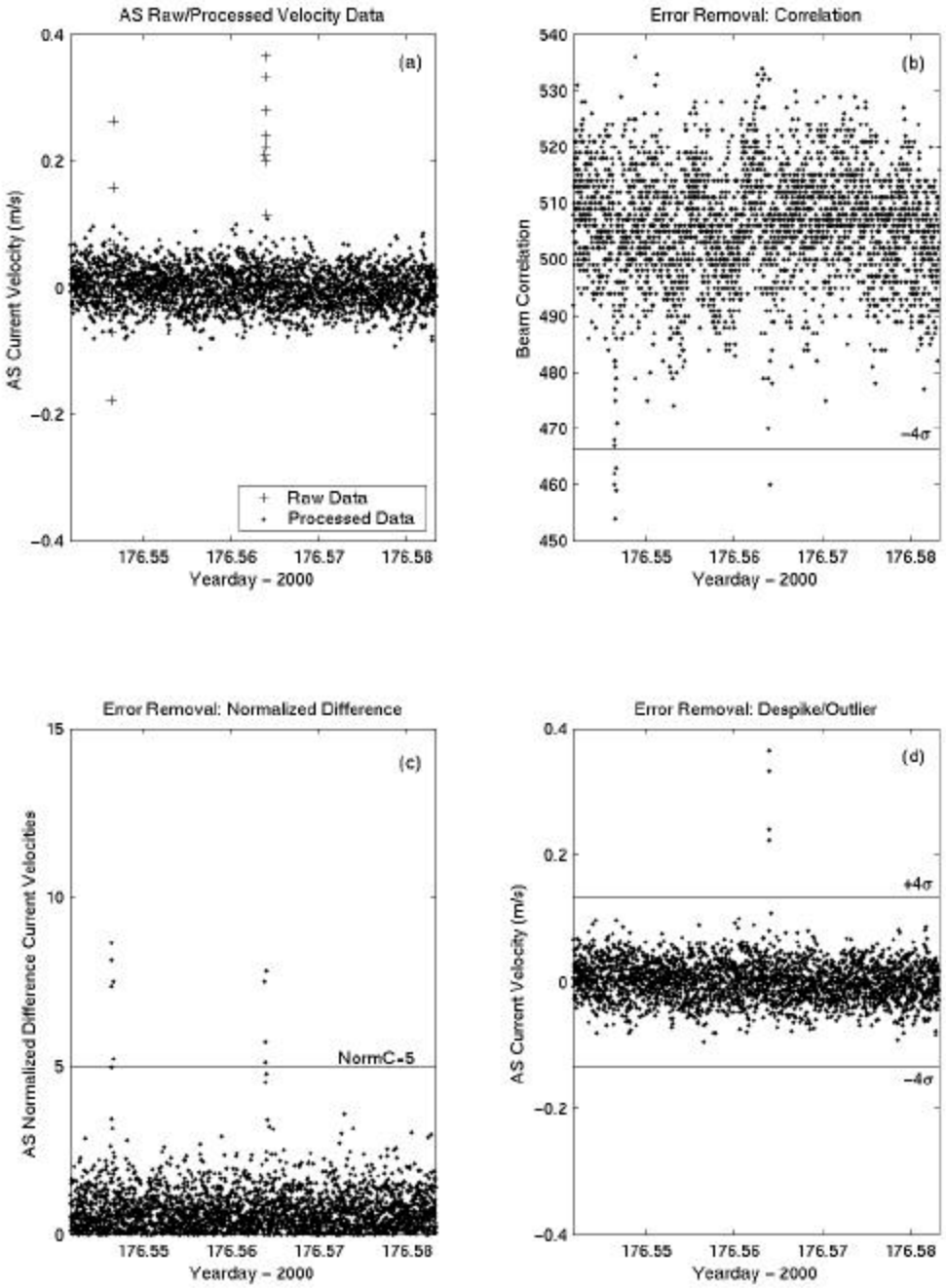

Figure 14. Error-removal sequence for the thirteenth hour of yearday 2000176 ADCP velocity data: (a) raw and processed data using the selected threshold levels, (b) ADCP beam correlation values with a 4σ threshold level, (c) normalized range bin difference using a cutoff value of 5, and (d) temporal difference despike/outlier corrected data using a 4σ threshold level.

the velocity distribution, and is calculated by dividing the third moment by the cube of the standard deviation. A skewness coefficient of 0 indicated equal oscillatory flow in either direction. A negative skewness (in the cross-shore direction) indicates a net offshore flow, while a positive skewness coefficient represents net on-shore flow. The kurtosis coefficient, or the ratio of the fourth moment to the variance squared, represents the peakedness or flatness of the velocity component time-series.

Using the time-series provided by the pressure sensor in the BADCP and by applying a linear wave theory transfer function to the surface, significant wave height ($H_{1/3}$) was calculated for each hour using the following equation:

$$H_{1/3} = 4 * s_{pressure} \tag{26}$$

where $s_{pressure}$ is the standard deviation of the pressure data for one hour scaled to m of water. Each hour's averaged pressure data was also used to monitor tidal fluctuations at the MISO site.

A Maximum Entropy Method (MEM) directional wave spectra algorithm based on *de Valk* [1990] and *Rockafellar* [1974] was applied to the 2m level ADCP (*p*, *u*, *v*) time-series in one-hour increments to obtain the mean wave direction, peak wave direction, peak period, and spectral width of the incoming waves. The Appendix outlines the procedure for obtaining the wave energy distribution from the MISO (*p*, *u*, *v*) data. This energy distribution was calculated over a frequency (f) range of $0.03 < f < 0.15$ Hz, and direction (q) bins of five degrees. The mean wave direction ($\overline{q_{wdir}}$) was calculated from the energy distribution function, *E(f,q)*, according to

$$\overline{q_{wdir}} = \frac{\int_{0.15}^{f} \int_{-p}^{p} E(f,q) q \, dq}{\int_{0.03}^{} \int_{-p}^{p} E(f,q) \, dq \, df} \tag{27}$$

The peak direction (q_p) was calculated by summing the energy into direction bins and locating the maximum energy content. Conversely, the peak frequency (f_{peak}) was determined by summing the energy distribution into frequency bins and locating the maximum energy content. The spectral width (W) was determined by

$$W = 2\sqrt{\left|\frac{M_2}{M_0}\right| - \left(\frac{M_1}{M_0}\right)^2} \tag{28}$$

where the moments M_0, M_1, and M_2 at the peak frequency and across all directions are

$$M_0 = \sum E\left(f_{peak}, q\right) \tag{29}$$

$$M_1 = \sum E\left(f_{peak}, q\right) * q_{COM} \tag{30}$$

$$M_2 = \sum E\left(f_{peak}, q\right) * q_{COM}{}^2 \tag{31}$$

as defined by the directional positions relative to the center of mass (q_{COM}).

Figure 15 shows the energy distribution across frequency and direction for one hour of an energetic winter day. The spectral energy is highly focused at a direction of approximately 090° and a f_{peak} of 0.0576 Hz (T_{peak} = 17s). The spectral width for this hour is ~13.1°. Figure 16 contains the energy distribution of a less-energetic summer day. Note that the energy distribution is spread across all directions in the 0.0667 Hz frequency bin (15s period), with a peak direction identified at 90°. Of particular interest is the apparent reflection of energy at 270°, 180° opposite of the peak direction.

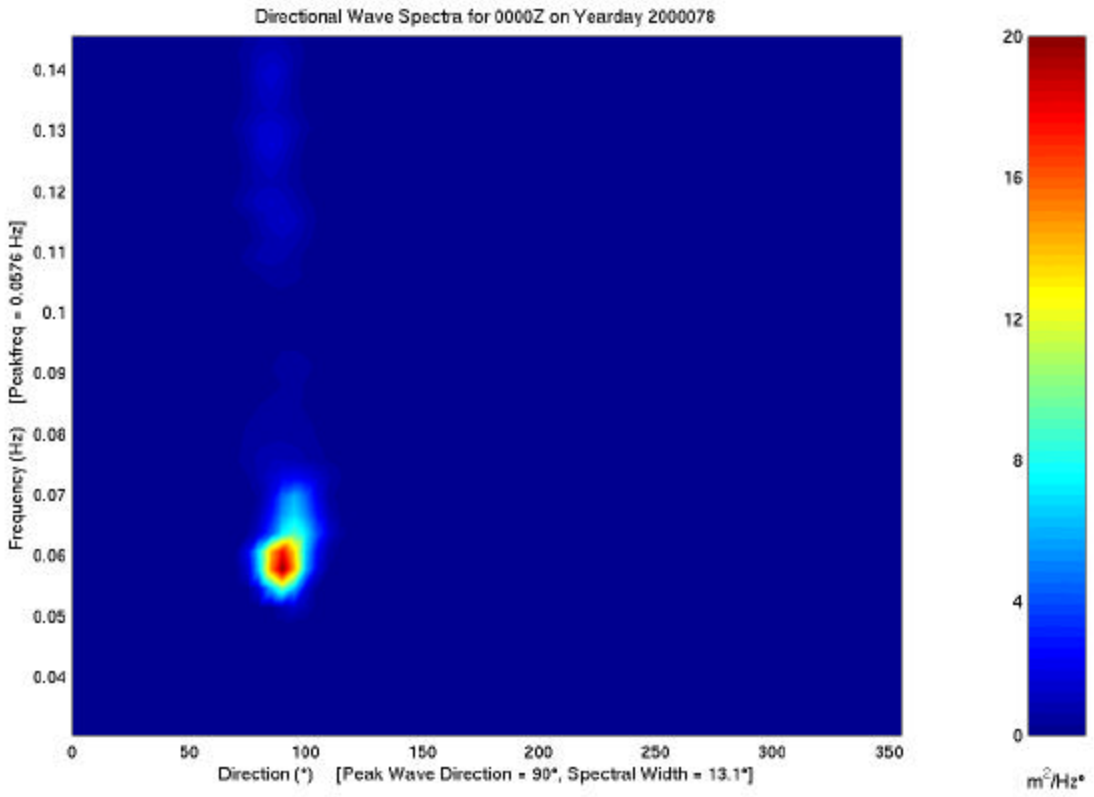

Figure 15. Wave energy for a high-energy winter yearday (2000078) according to frequency and direction. Note the highly focused energy concentration at 90°, and the low spectral width.

To ensure that reflected energy was not included in spectral width calculations, spectral widths were only calculated from θ_p-90° to θ_p+90°. The spectral width for this day given these constraints was a large 70°.

Infragravity wave energy was estimated from the corrected 2m height velocity component time-series for each hour by low-pass filtering the velocity time-series with a fourth order, digital Butterworth filter with a 30-s cutoff to remove wave velocities and retain only infragravity motions. RMS quantities due to infragravity motion were calculated to characterize the level of infragravity forcing found at the MISO site.

The wave orbital radius (d_r) was estimated from the time integration of the wave-frequency energy by applying the $1/jw$ operator in the frequency domain and integrating across the wave frequencies:

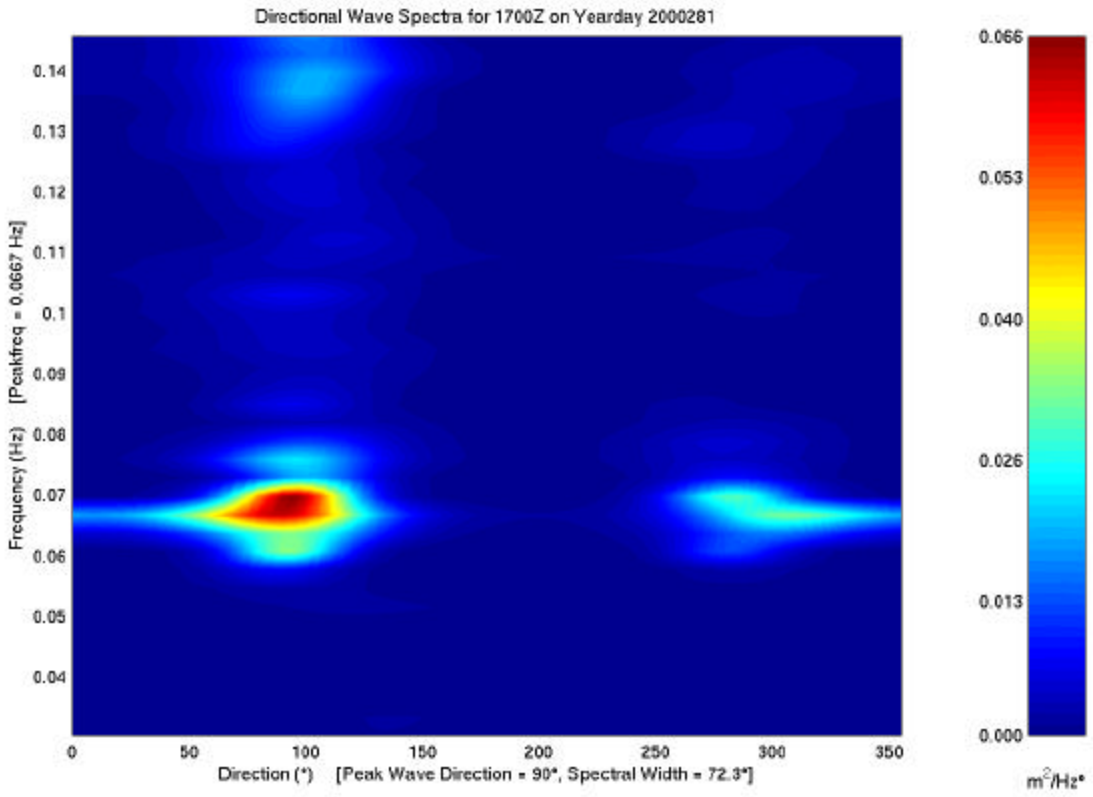

Figure 16. Wave energy for a low-energy (note the scale change in energy magnitude from figure 15) summer yearday (2000281) according to frequency and direction. Note the spread of energy across all directions and the large spectral width. Also of interest is the reflection of energy 180° opposite the peak wave direction of 90° at 270°.

$$d_{r(u,v)} = \sqrt{\int_{0.03}^{f_N} \left(1/w\right)^2 * S_{xx}(f)\,df} \qquad (32)$$

where $w = 2pf$, f_N is the nyquist frequency, and $S_{xx}(f)$ is the autospectrum of each hour-long velocity component time-series. A 30-s high-pass cutoff has been selected here. The wave orbital diameter (d_o) was calculated from the magnitude of both velocity components' radii:

$$d_o = 2\sqrt{{d_{r,u}}^2 + {d_{r,v}}^2} \tag{33}$$

where $d_{r,u}$ and $d_{r,v}$ are the cross-shore and alongshore wave orbital excursion radii, respectively.

Sediment transport is governed by (among other factors) the bottom stress. Bottom stress can be divided into two components: form drag and skin friction, where skin friction is primarily responsible for sediment motion. Using the RMS and mean velocity magnitudes, the bottom stress was calculated from both wave (t_w) and current (t_c) components:

$$t_b = t_w + t_c = \frac{1}{2} r f_w \left({U_{RMS}}^2 + {V_{RMS}}^2\right) + \frac{1}{2} r f_c \sqrt{{U_m}^2 + {V_m}^2} \tag{34}$$

where r is the density of seawater, U_{RMS} and V_{RMS} are the wave RMS component quantities, U_m and V_m are the mean current component quantities, and f_w and f_c are wave and current friction factors, respectively. The wave friction factor f_w is modeled after Jonsson (1966) as

$$f_w = \exp\left(5.213\left(\frac{2.5D_{50}}{0.5d_o}\right)^{0.194} - 5.977\right) \tag{35}$$

where D_{50} is the median grain diameter of 0.260 mm. The current friction factor used in equation 12 is estimated as $f_c = 0.003$ following Amos et al., 1988.

The Shields parameter was utilized to determine the point when sediment motion was initiated and to predict sediment transport. It represents the ratio of the bed shear stress to the immersed weight per unit area, and is estimated by

$$q' = \frac{t_b}{r(s-1)gD_{50}} \tag{36}$$

where *s* is the ratio of sediment grain density to water density (2.65 for quartz sand), and *g* is the gravity acceleration.

B. SCANNING ACOUSTIC ALTIMETER

1. Data Acquisition

A scanning Acoustic Altimeter (SAA) (*Stanton*, 2000), developed by the ocean turbulence research group at the Naval Postgraduate School, continuously mapped the sandy bed in a 1m alongshore by 1.5m cross-shore area immediately offshore from the MISO frame. This high-resolution altimeter consisted of a transducer head mounted on a 2-axis stepper motor that directed the altimeter transducer toward the ocean bottom in alongshore (x) and cross-shore (y) directions offset by 12° from the ADCP orientation (Figure 6). An onboard microprocessor processed the acoustic data, found the bed range, and controlled the motors as the SAA scanned in 1° increments over a ±35° span in each axis, allowing the changing bumps and ripples on the bed to be measured even in optically opaque, turbid water conditions. The SAA began its sampling by starting at a centerline and stepping rapidly back and forth cross-shore while incrementing the alongshore angle at the end of each cross-shore pass. Upon completion of this half of the area scan, the SAA returned to the centerline and progressed out to the left, sampling each point with 20 pulses of 1.3 MHz sound waves. By oversampling spatially and using an Objective Analysis technique, a gridded z(x,y) map and an error map of center weighted averages of data within a 6 cm diameter Gaussian field at each grid-point was created. This resulted in a regular, smoothed morphology map with a 1.2 cm increment in x and y with a 3 cm half power bandwidth. Ripple wavelengths of 0.03 to 1.2 m were resolved in these maps. Figure 17 shows typical spatial sampling positions of the raw bed elevations before gridding using an Objective Analysis.

The sampling time for each map was typically around 15-20 minutes, with the sample frequency determined by the acoustic turbidity and near-bed sediment motion. At any given time, if there were large amounts of suspended sediment or air bubbles in the water column preventing a bed detection, the SAA would retry three times before incrementing to the next scan position.

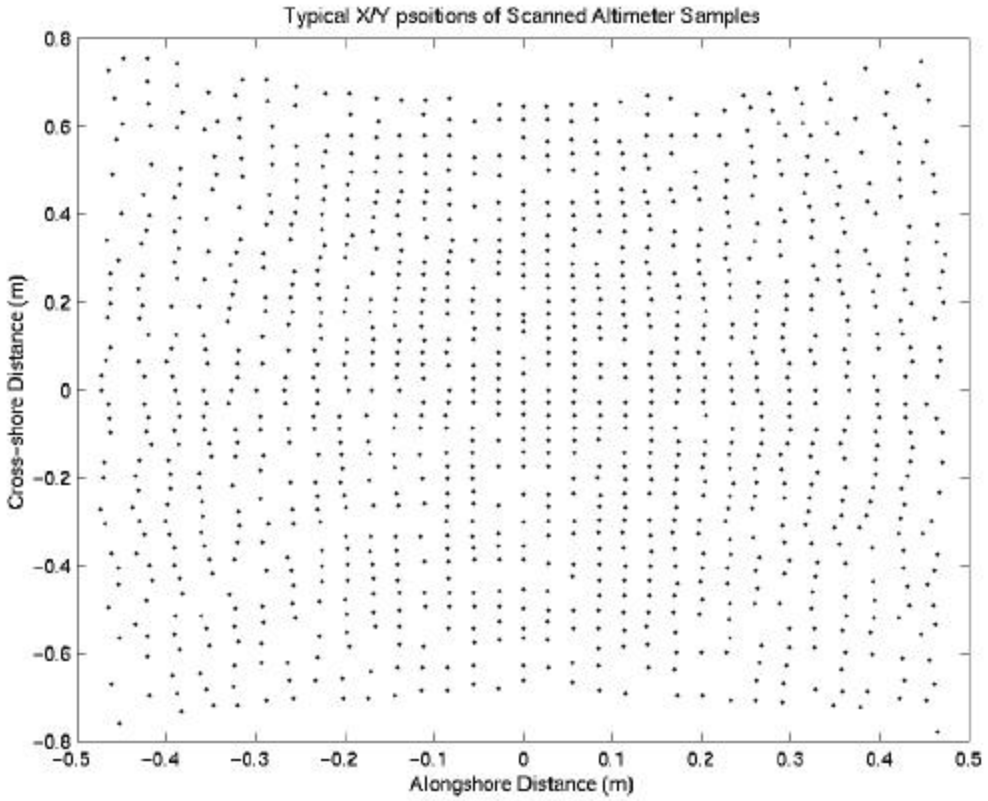

Figure 17. An output grid of x/y positions from the Scanning Acoustic Altimeter (SAA) following processing. Note the ripples on the left and right side of the map, observed by the relative closeness of the x/y points.

2. Data Processing

In order to best characterize the bed's geometry from the SAA maps and its response to wave and current forcing, it is necessary to distinguish relic ripples from active cases. Ripples can be present on sandy beds over a wide range of flow conditions extending from minimum shear velocities necessary to initiate sediment motion up to water flows intense enough to produce sheet flow sand motion, eliminating any ripple formations. As the wave and current forcing begin to increase over a planar bed, sand grains suspended in the water column by mean currents begin to settle and align with each other in ridges perpendicular to the direction of oscillatory flow. These ridges increase in spacing and become more asymmetric as vortices form on the ridges' lee side under increased flow. The previously planar bed has now been transformed into a field of long-crested, asymmetric ripples typically observed during periods of moderate wave and current forcing. As strong forcing conditions subside, and the flow conditions significantly decrease, the ripples cease to grow or migrate and become relict. Once the wave energy increases again, small wavelength ripples begin to form on the long wavelength relic ripples. To understand the relationships between the forcing and bed response during these changing forcing conditions, it is necessary to correctly isolate the geometry of the actively growing ripples, which are typically atop large unchanging relic ripples. The following method was utilized to make this distinction and correctly identify the wavelength and height of actively growing ripples.

Using a two-dimensional FFT, a ripple height variance (η^2) spectrum was calculated for each OA grid map in wavenumber component (k_x, k_y) space. These maps were averaged into one-hour time intervals to coincide with the wave and current forcing statistics calculated from the BADCP data. Gaps not longer than six hours in the mapped η^2 time-series were interpolated across using a linear interpolation scheme.

To reduce the effects of noise in the η^2 variance spectrum, all η^2 values below a determined threshold level were rejected and removed from the spectral bins. A noise threshold level of 4×10^{-8} m^2 was determined from η^2 variances at high wavenumbers during quiescent conditions under the assumption that white noise existed across the entire time-series. Figure 18 displays the η^2 time-series used in the selection of the noise

level threshold. Nine bins of high wavenumber (14.1-16.5 m^{-1}) η^2 values collected during 32 calm, low-energy days (768 hours) contributed to this time-series. An active ripple limit (above which ripples may legitimately be forming) was conservatively chosen at 0.75×10^{-7} m^2. Any η^2 values above this limit did not contribute to the noise threshold calculations. The points below this limit were averaged to determine the noise floor for the entire mapped η^2 time-series.

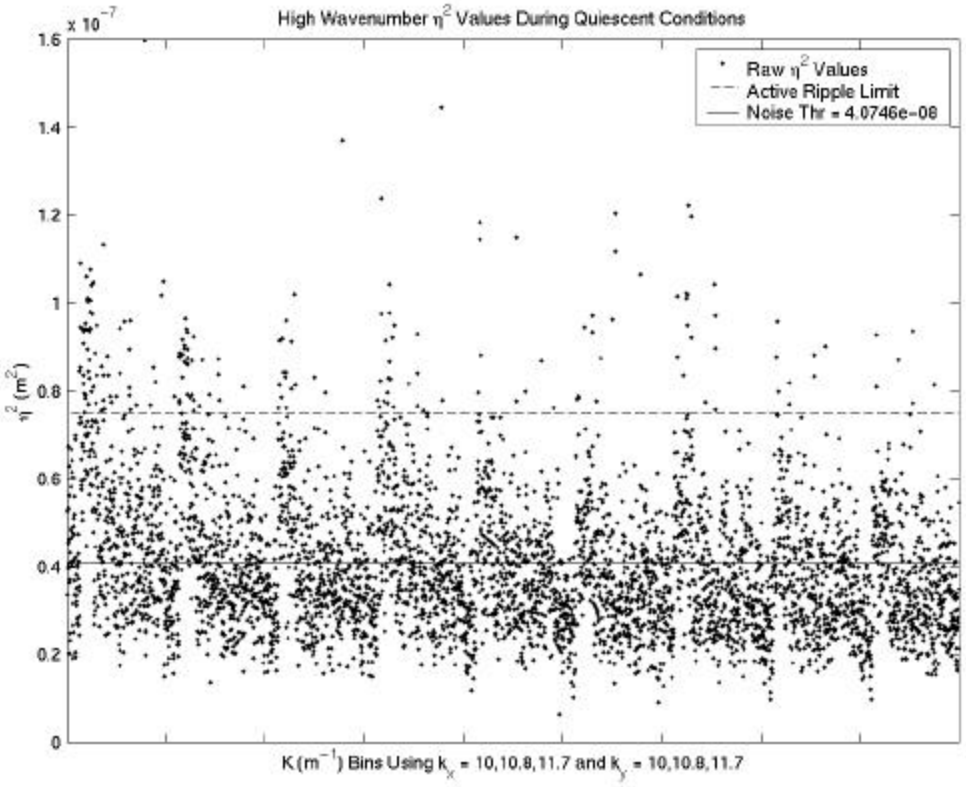

Figure 18. η^2 time-series used to determine the noise threshold level for the η^2 variance spectrum derived from the Scanning Acoustic Altimeter (SAA) objective analysis maps. Excluding η^2 values beyond an active ripple limit of 0.75×10^{-7} m^2, nine bins of high wavenumber (14.1-16.5 m^{-1}) η^2 values collected during 32 calm, low-energy days were averaged to determine the noise floor of 4×10^{-8}.

Following the removal of all η^2 values below the noise threshold, each (k_x, k_y) η^2 value was normalized by its bin's corresponding mean across all time in (k_x, k_y, t) space:

$$h^2_{norm}(k_x, k_y) = \frac{h^2(k_x, k_y)}{h^2(k_x, k_y)} \quad (37)$$

A slew rate (δ) for each (k_x, k_y) combination was then calculated by forming a ratio of differenced normalized η^2 values to time:

$$d(k_x, k_y) = \frac{\partial h^2_{norm}(k_x, k_y)}{\partial t} \quad (38)$$

A fourth order low-pass digital Butterworth filter with a six hour cutoff was applied to these slew rates to retain the six hour and longer changes in spectral energy in order to detect significant temporal changes as the ripple field evolved.

Active ripple growth periods were identified whenever the slew rates exceeded a threshold level of 3.25 m^2/hour. Figure 19 provides an illustrative example of this threshold selection using the time-series of one wavenumber (K = 3.00 m^{-1}). The 3.25 threshold level (Figure 19(c)) identified four periods of ripple growth during days 1-2, 9-11, 14-15, and 27-28. Decreasing the threshold level to 2.25 and 1.25 (Figure 19(a,b)) increased the number of active ripple detections by accepting more closely-spaced successive h^2_{norm} values. Conversely, by increasing the threshold level to 4.25 (Figure 19(d)) and beyond, large differences in successive h^2_{norm} values were required for active detection, resulting in sparse identifications of active ripples. For these reasons, slew rates exceeding a threshold of 3.25 were used to define ripple growth for each $\eta^2(k_x, k_y)$.

To ascertain the ripple geometry during these periods of growth, the η^2 variance spectrum was binned by direction into alongshore and cross-shore sectors as well as by a

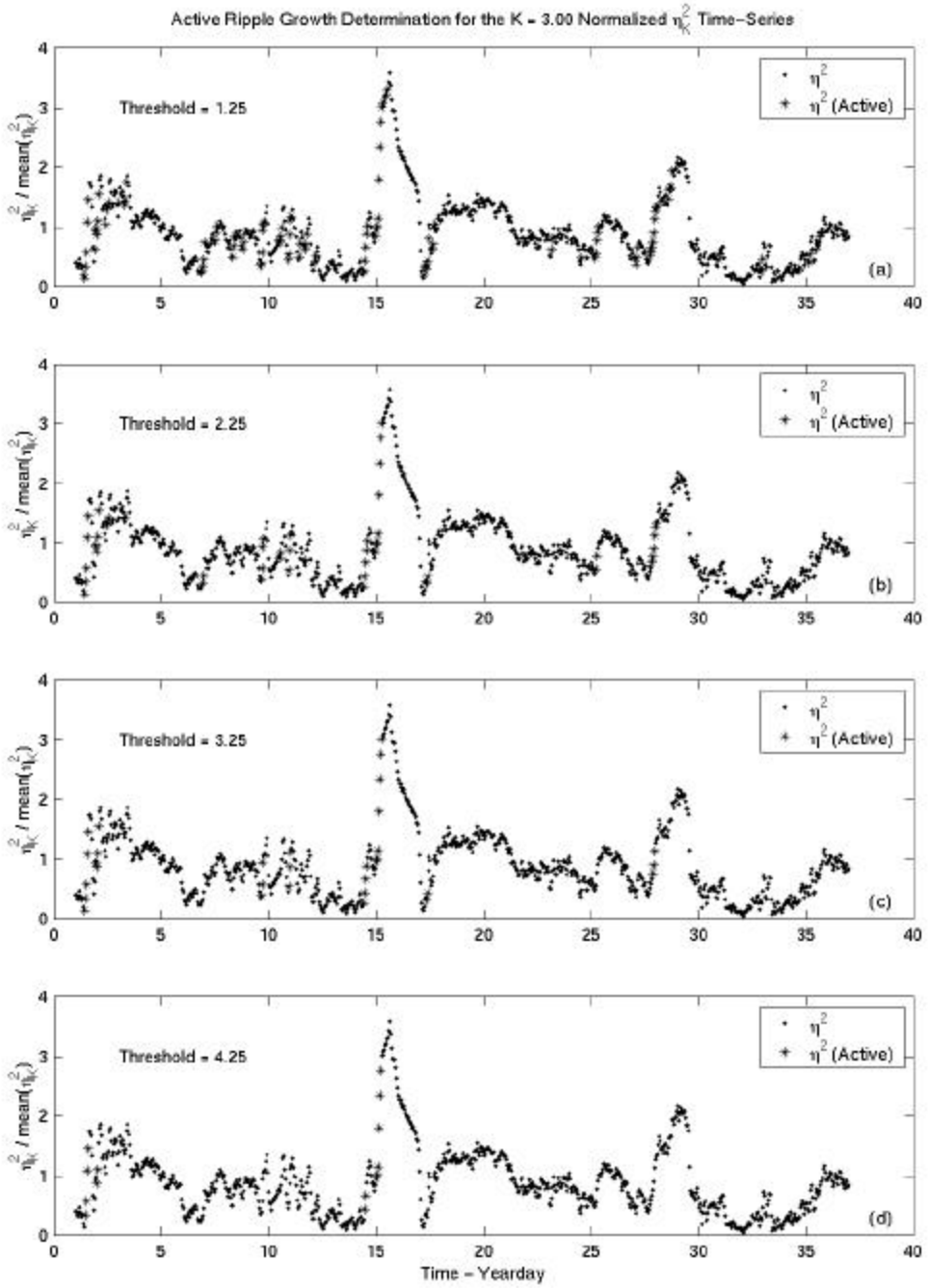

Figure 19. Threshold selection for discerning active ripple growth from relic ripple states as applied to the normalized η^2 variance time-series of K = 3.00 m^{-1}.

radial-binned wavenumber. Mapped η^2 values within the alongshore (0-45°) and cross-shore (45°-90°) sectors were then binned into fifteen evenly spaced, weight-averaged, composite, radial wavenumber bins ranging from 0.83 m^{-1} to 11.67 m^{-1}. Time-series of alongshore and cross-shore η^2 variance for fifteen wavenumbers were obtained in this manner. Time-series of η^2 values identified as active according to the filtered slew rates were also obtained. If an η^2 value was identified as being an active point within a direction bin's wavenumber bin, all η^2 values in that wavenumber bin were removed and summed, thus producing fifteen η^2 sums (0 in place of inactive cases). From this wavenumber distribution of η^2, the ripple wavelength and height can be calculated according to the weighted centroid of the maximum variance contribution and its two adjacent variance values.

THIS PAGE INTENTIONALLY LEFT BLANK

IV. RESULTS AND ANALYSIS

The wave and current forcing time-series for year 2000 are shown in Figure 20. Mean currents in the alongshore direction (not shown) with peaks of up to 22 cm/s are stronger than the weaker tidal currents in the cross-shore direction (Figure 20(a)) with peaks up to 8 cm/s. The cross-shore RMS wave velocities (Figure 20(b)) reached peaks of 20-30 cm/s during the winter (Days 1-100), reducing to 5-10 cm/s during the spring and summer months (Days 101-250). Peak periods (Figure 20(d)) reached 13-20s during the stormy winter months, and 10-15s during calmer summer conditions. The spectral widths (Figure 20(e)) of incident wave energy at the MISO site changed from narrow-band ranges averaging 20° during the winter to 35° spreads during the summer. Wave orbital velocities (Figure 20(f)) reached peaks of 1-2m during periods of high oscillatory flow in the winter, and reduced to < 0.5m with decreased wave forcing during the summer. The Shields parameter representing the combined wave and current flow's ability to move the sediment and induce ripple formation is plotted in Figure 20(g). A critical Shields parameter of $q'_{crit} = 0.04$ (*Amos et al.*, 1988) shows an approximate threshold level for sediment motion. The Shields parameters exceeded q'_{crit} during periods of intense wave and current forcing in the winter with values ranging up to 0.15. During the summer, the bottom stress due to waves was less than during winter conditions, producing Shields parameters < 0.07 and largely below q'_{crit}.

Using these forcing characteristics as an indication for the possibility of ripple formation and upon inspection of the alongshore and cross-shore active wavenumber binned η^2 variance time-series, active ripple conditions were identified frequently through the winter days, while relict ripples dominated the more quiescent summer periods. The focus of this investigation is to understand the processes that transform the bed by actively building ripples. For this reason, three representative cases of evolving wave and current forcing events from the winter time period are presented and analyzed. A representative example from the summer is also provided for contrast.

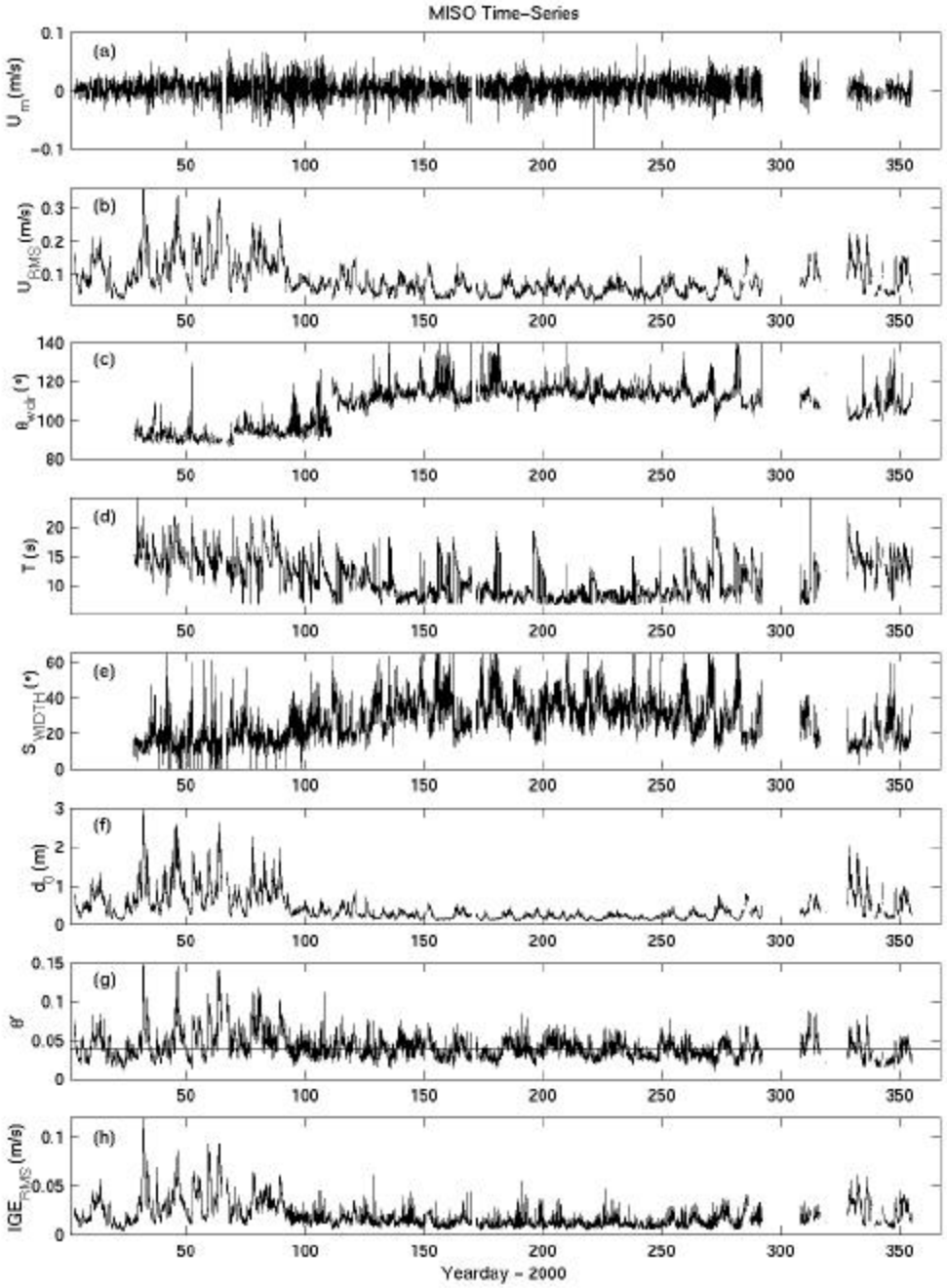

Figure 20. MISO time-series: (a) cross-shore mean currents, (b) cross-shore wave velocities, (c) mean wave direction, (d) peak period, (e) spectral width, (f) wave orbital diameter, (g) shields parameter, and (h) cross-shore infragravity RMS.

Wave and current forcing time-series from days 50-54 (Figure 21) demonstrate the potential for ripple growth under increasing wave forcing conditions. Between days 50-52, low orbital velocities, high wave orbital diameters, and sub-critical Shields parameters were observed. The direction/wavenumber binned η^2 variance time-series at the start of this time-series (50-50.3) indicate that the ripple field grew to be dominated by cross-shore 0.6 m to 1.2 m orbital ripples (Figure 22(a)). Ripple wavelength predictors proposed by *Nielsen* [1981] (equations 1 and 5), and *Clifton and Dingler* [1984] (equation 10) illustrated similar bed responses to the forcing conditions during this time (Figure 29, upper panel). Both the wave-dominated *Wiberg and Harris* [1994] model (equations 10-15) and the combined-flow *Khelifa and Oullet* [2000] model (equation 16) predicted lower wavelengths below 0.4 m. Between 50.3 and 52.4, the wave forcing reduced below q'_{crit}, leaving relict ripples with these wavelengths and heights.

Between days 52.4 and 52.6, there was rapid alongshore growth in 0.2-0.6m ripple wavelengths as the orbital diameter rapidly increased to the sub-orbital range. Interestingly, the q' was just sub-critical during this time period, but clearly the bed was active. As the Shields parameter transitioned above critical during day 52.6, active ripple growth ceased in the alongshore direction, while the pre-existing 0.6 m relict orbital ripples in the cross-shore direction were decreased in height, with 0.4 m ripples growing in their place. This transition occurs at the start of predicted anorbital motion (Figure 22(c)). *Khelifa and Oullet's* [2000] combined flow model provides the closest prediction estimates of wavelengths around 0.4 m, while *Nielsen's* [1981] wave-dominated models and *Wiberg and Harris'* [1994] predictors estimated wavelengths around 0.8 m.

Days 28-31 provide a similar example of alongshore ripple growth (Figure 24(b)), but with a more gradual and lower increase in wave energy. Throughout the first day, there is sporadic growth in both the alongshore and cross-shore directions at 0.2, 0.24, and 0.3 m wavelengths during a period of marginally sub-critical q'. At 29.1-29.5, there was rapid alongshore growth as the wave forcing gradually increased from 0.1 to 0.15 m/s (Figure 23) and the wave orbital diameter entered the suborbital range (Figure 24(c)). The alongshore growth at this time was dominated by 0.4 m λ ripples with smaller levels

of growth at 0.2 and 0.24 m λ. Growth around 0.4 m wavelengths was predicted by several models including *Khelifa and Oullet* [2000] and *Clifton and Dingler* [1984] (Figure 30). As in the previous example of days 50-54, alongshore growth terminated upon the transition above q'_{crit} around day 29.6 of the 28-31 time period. From day 29.6-30.6, q'_{crit} remains above critical while cross-shore 0.6 and 1.2 m ripple growth is observed, coinciding with a rapid decrease of short wavelength ripples in the alongshore sector. Interestingly, the large 1.2 m λ alongshore ripple energy remained. At this point in the time-series, the observed wavelengths depart from those predicted by *Khelifa and Oullet's* [2000] model, and more closely resemble those predicted by *Wiberg and Harris'* [1994] suborbital λ equation (15) (Figure 30, upper panel) as the d_o / d_{50} ratio for this period of change fluctuates between suborbital and anorbital conditions.

Days 75-77 provided an example of a very slow wave forcing increase where q' remained at the critical level (Figure 25). Ripple growth was observed in both alongshore and cross-shore sectors (Figure 26(a,b)) during largely orbital conditions (Figure 25(c)). Similar to the previous two cases, increases in alongshore 0.2-0.4 m ripples were observed (days 75.4-75.7). *Khelifa and Oullet* [2000] adequately predict this increase under combined flow, while more rapid growth is estimated by Nielsen [1981] and *Wiberg and Harris* [1994] (Figure 31). Unlike days 50-54 and 28-31, however, this alongshore growth occurred during conditions where $q' > q'_{crit}$. Cross-shore 0.6 and 1.2 m ripple growth dominated the binned η^2 spectrum during peak orbital velocities of 0.14 m/s during 75.7-76.2, however, and these ripples were slowly decreased between 76.2-88 as orbital velocities and displacements lowered slightly. *Nielsen's* [1981] field data equation (5) and *Wiberg and Harris'* [1994] suborbital equation (15) provided the closest predictions of this evolution. *Khelifa and Oullet's* [2000] as well as *Clifton and Dingler's* [1984] wavelength equations (16 and 8, respectively) overestimated the bed's response to wave and current forcing.

Ripples produced during relatively calm conditions of a representative summer period provide an interesting contrast to the actively changing bedforms indicative of strong winter forcing. Days 270-274 illustrate a long period of ripples in a relict state as

typically observed for the summer months (Figure 28). As the orbital motion begins to increase and q' transitions above critical (Figure 27), alongshore ripples ranging from 0.3-0.4 m were produced around day 274 and 275.4. All wavelength predictors initially provide estimates of relic ripple states during days 270-272 (Figure 32). At day 272, a slight increase in wavelength is predicted for all models. During the period of active ripple growth (day 274-275.4), *Khelifa and Oullet* [2000] once again predict wavelengths comparable to those observed from the MISO time-series. The *Clifton and Dingler* [1984] and *Wiberg and Harris* [1994] models produce similar results, while *Nielsen's* [1981] ripple wavelength predictor overestimates wavelengths by 0.2m.

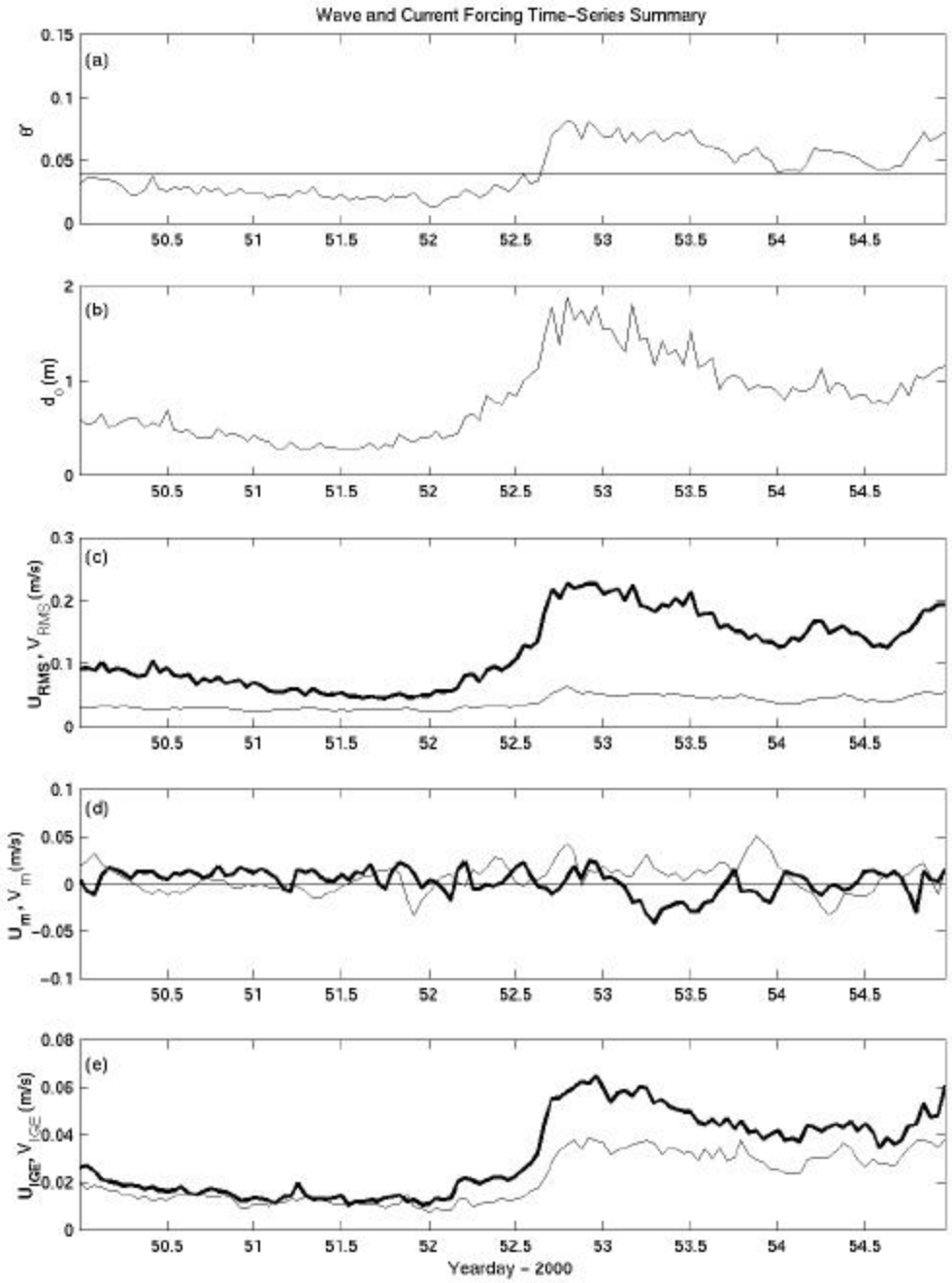

Figure 21. Wave and Current forcing time-series for days 50-55: (a) Shields parameter, (b) wave orbital diameter, (c) wave orbital velocities, (d) mean currents, and (e) infragravity RMS velocity.

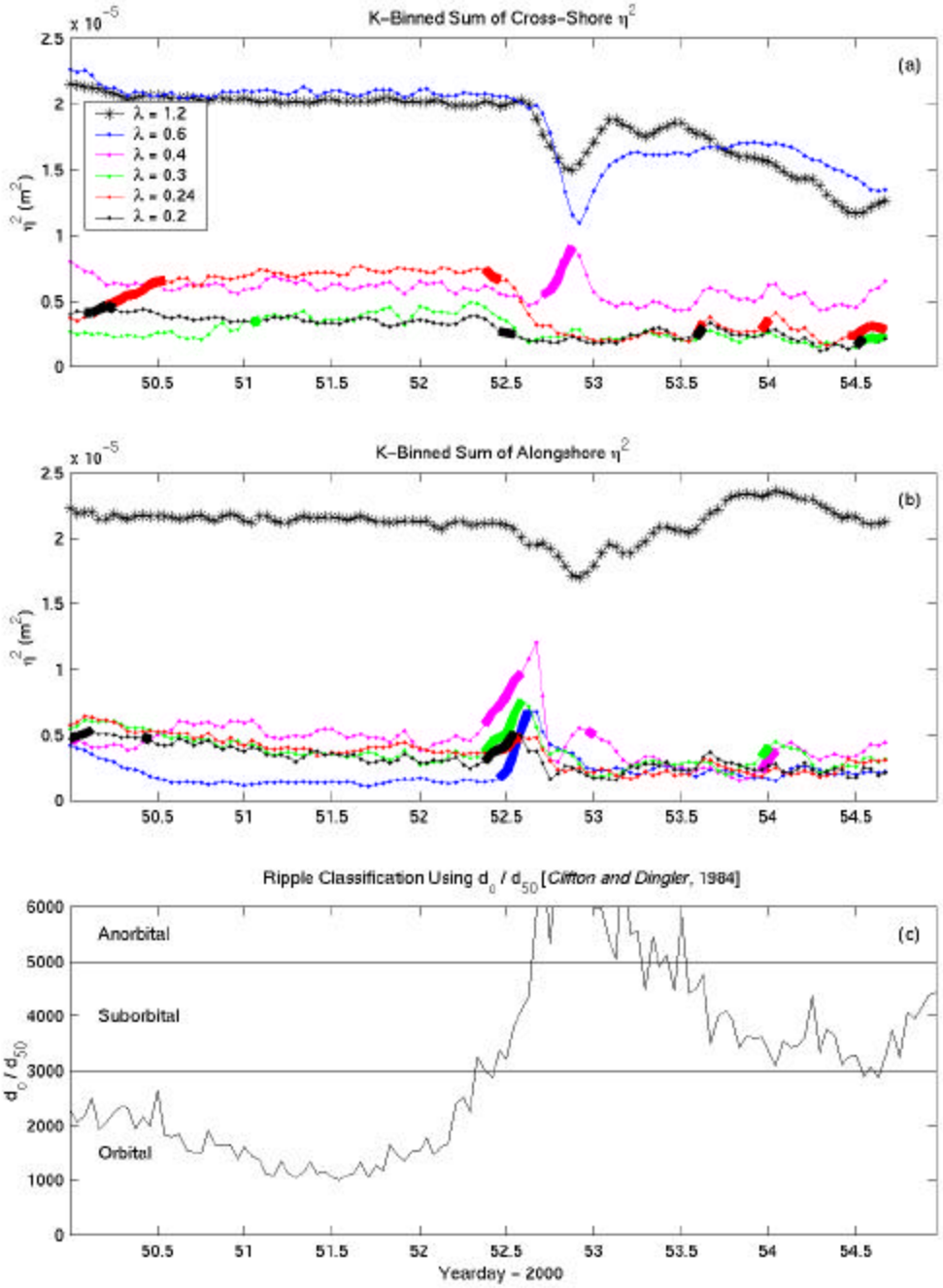

Figure 22. Bed response time-series for days 50-55: (a) wavenumber binned η^2 (cross-shore), (b) wavenumber binned η^2 (alongshore), and (c) ripple type classification.

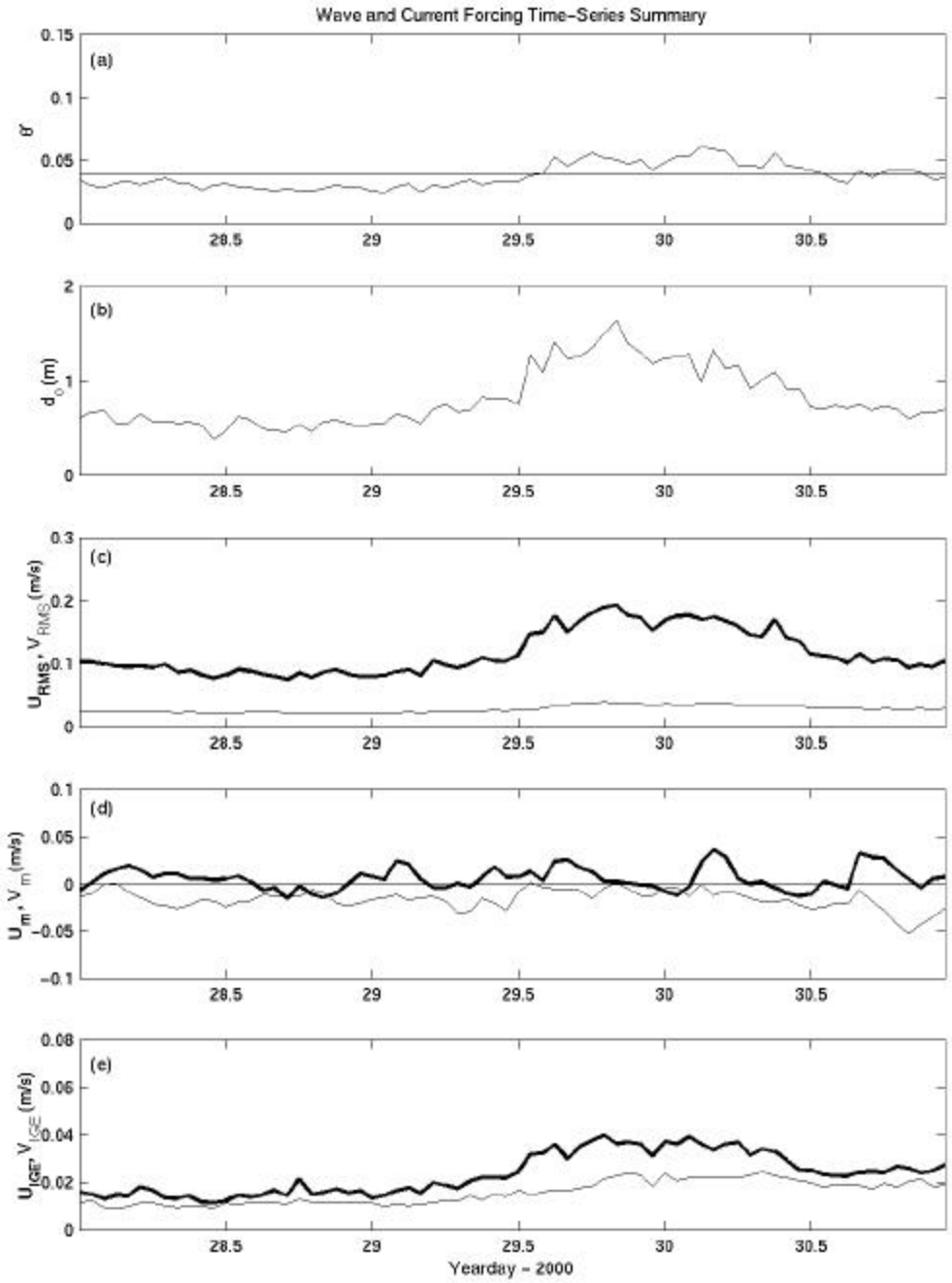

Figure 23. Wave and Current forcing time-series for days 28-31: (a) Shields parameter, (b) wave orbital diameter, (c) wave orbital velocities, (d) mean currents, and (e) infragravity RMS velocity.

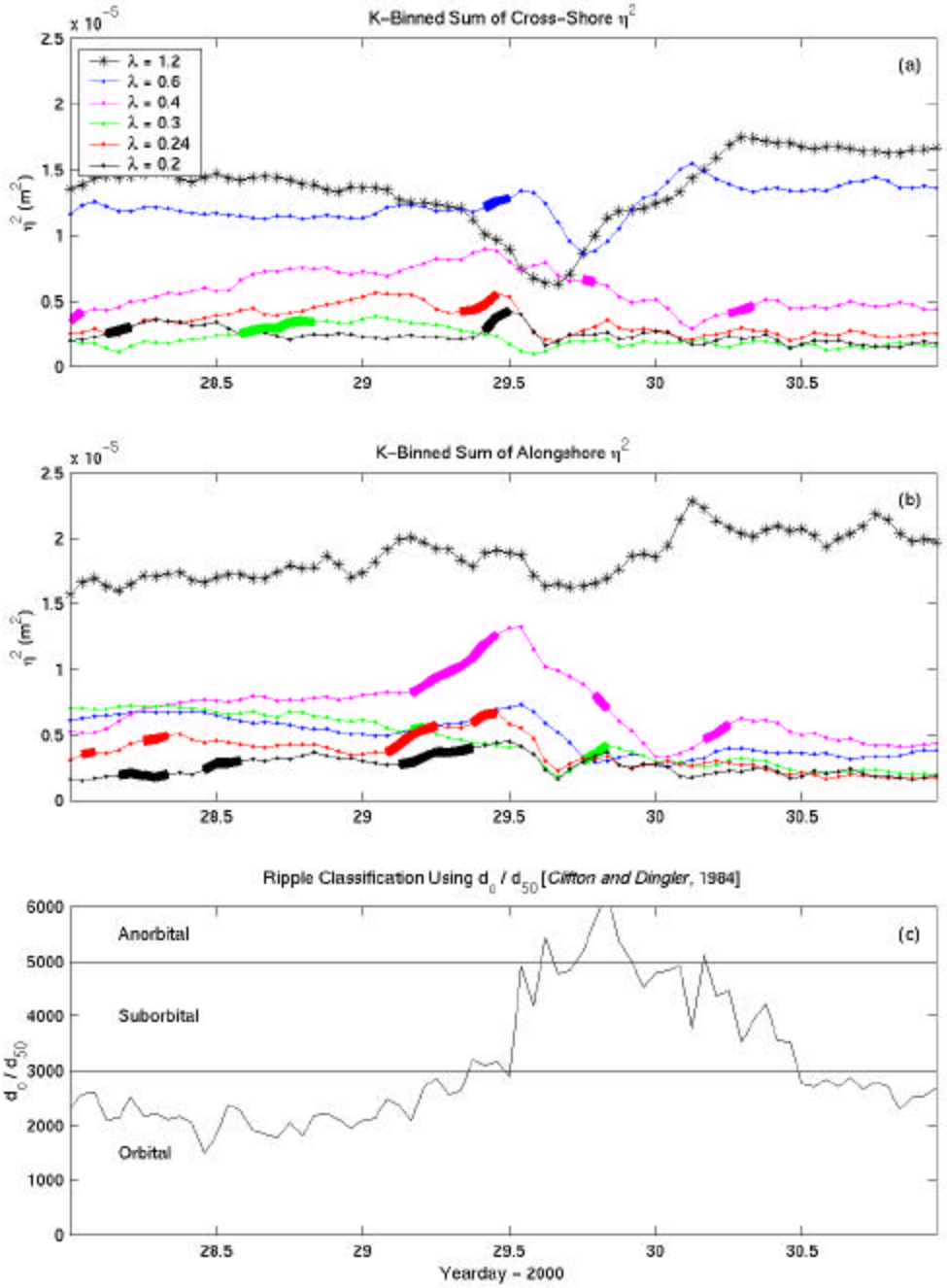

Figure 24. Bed response time-series for days 28-31: (a) wavenumber binned η^2 (cross-shore), (b) wavenumber binned η^2 (alongshore), and (c) ripple type classification.

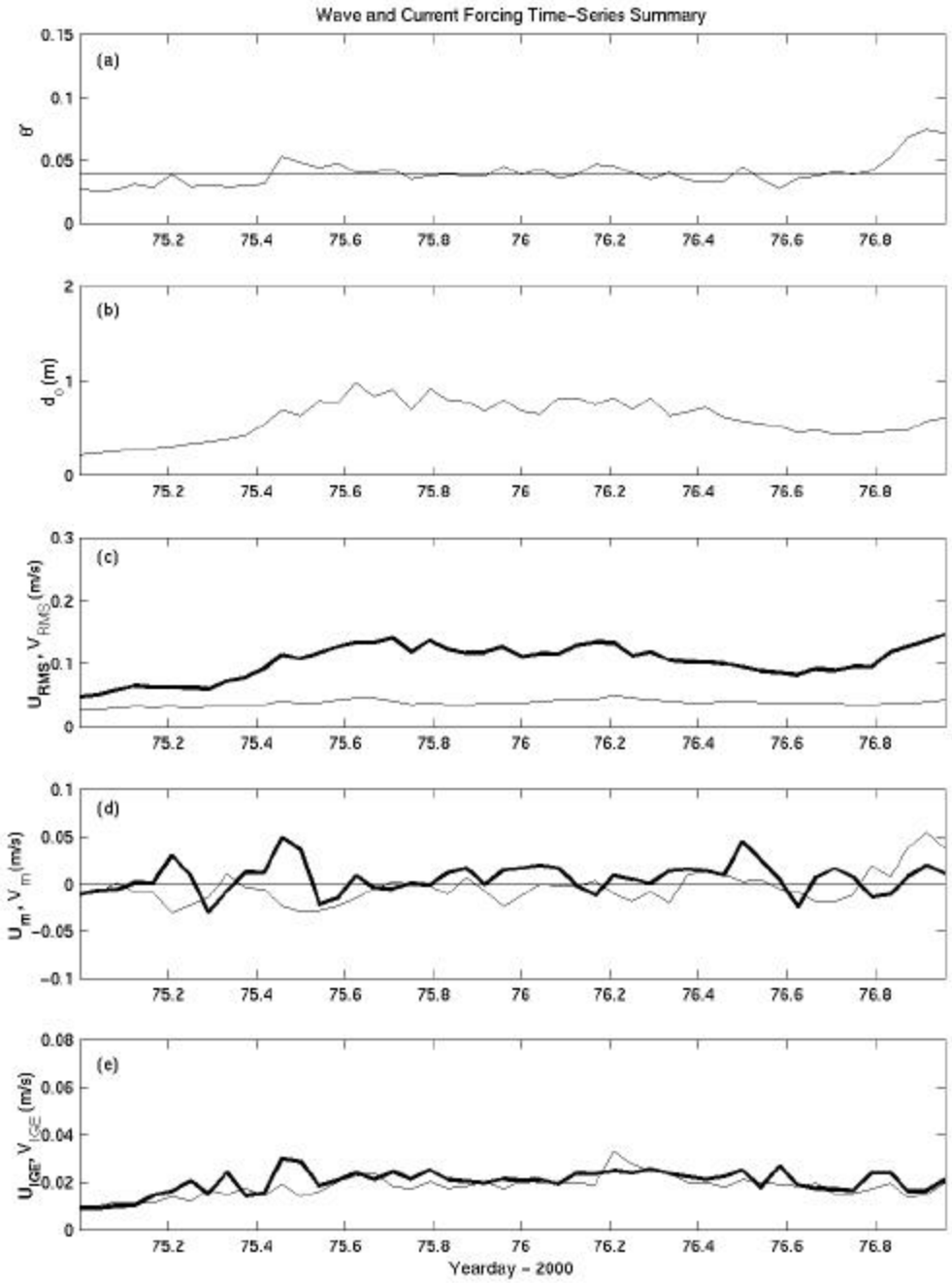

Figure 25. Wave and Current forcing time-series for days 75-77: (a) Shields parameter, (b) wave orbital diameter, (c) wave orbital velocities, (d) mean currents, and (e) infragravity RMS velocity.

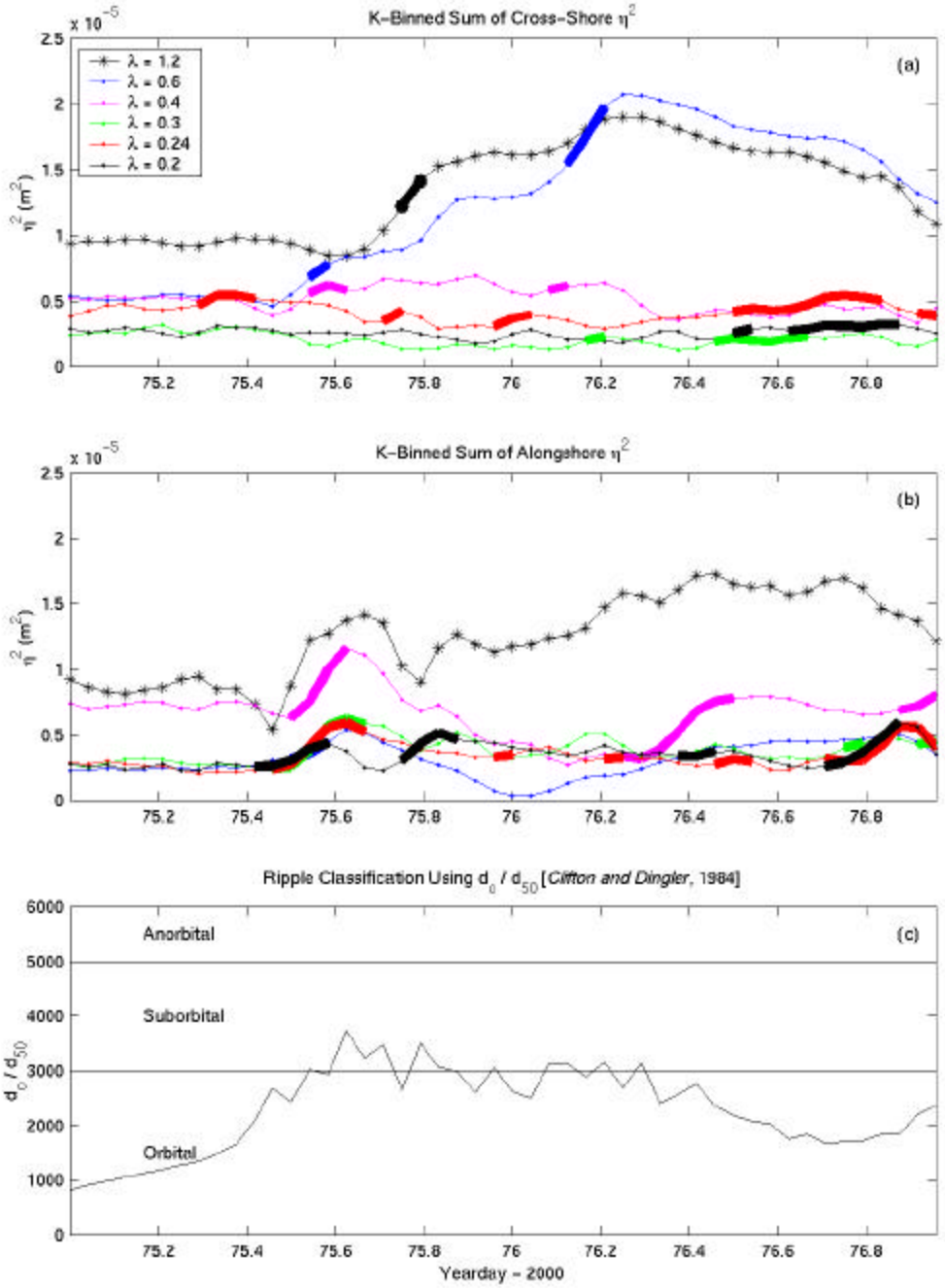

Figure 26. Bed response time-series for days 75-77: (a) wavenumber binned η^2 (cross-shore), (b) wavenumber binned η^2 (alongshore), and (c) ripple type classification.

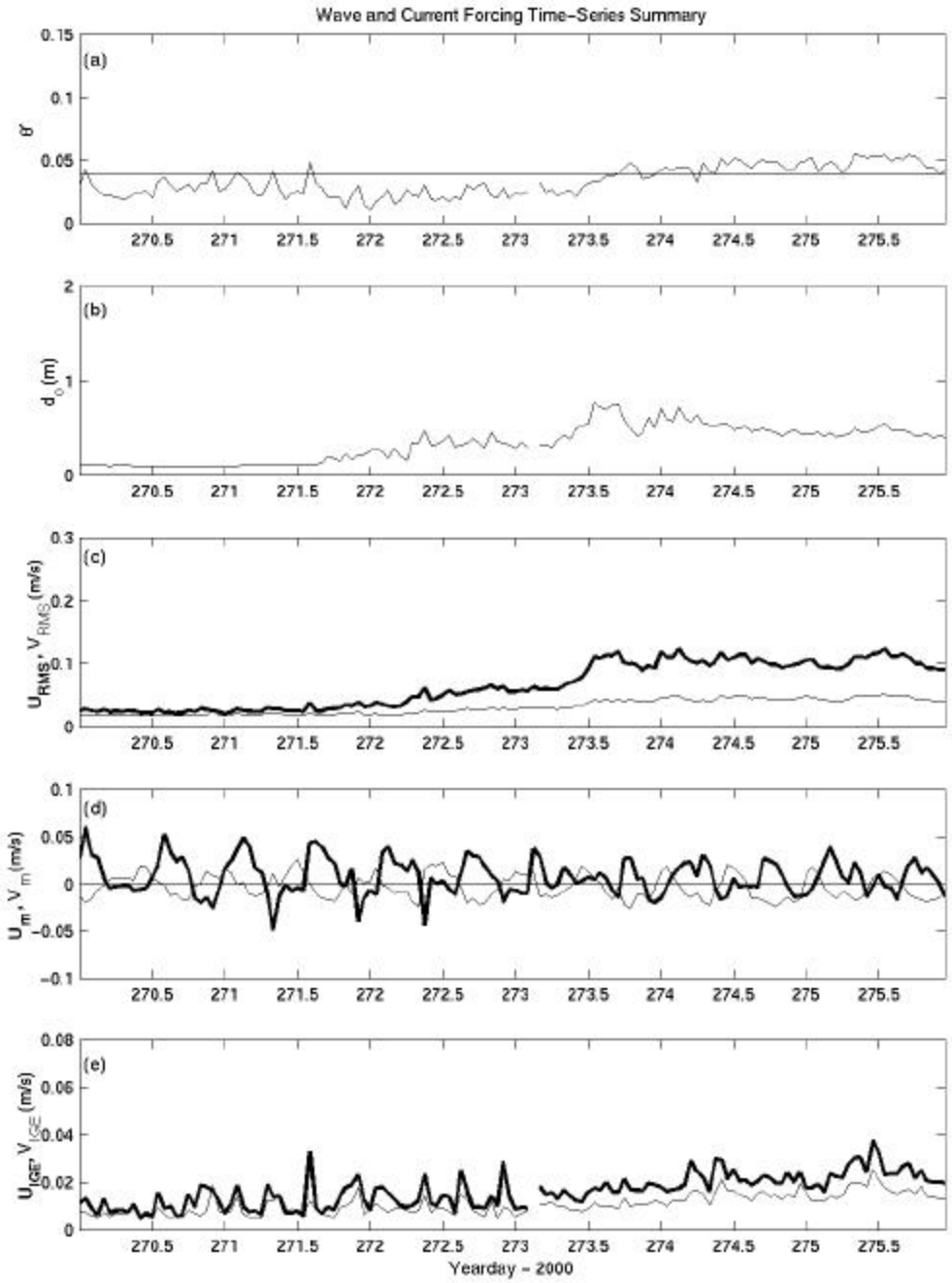

Figure 27. Wave and Current forcing time-series for days 270-276: (a) Shields parameter, (b) wave orbital diameter, (c) wave orbital velocities, (d) mean currents, and (e) infragravity RMS velocity.

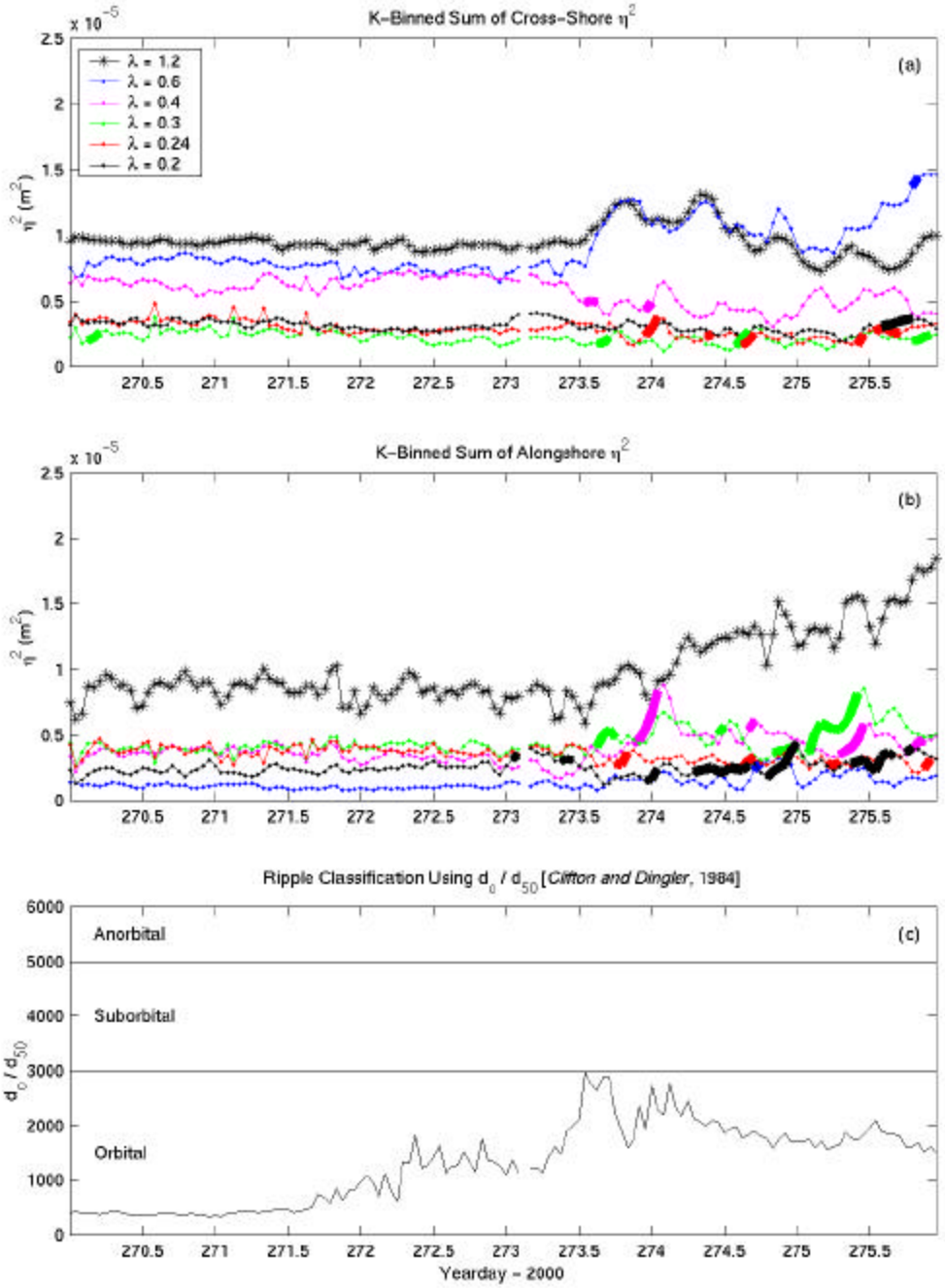

Figure 28. Bed response time-series for days 270-276: (a) wavenumber binned η^2 (cross-shore), (b) wavenumber binned η^2 (alongshore), and (c) ripple type classification.

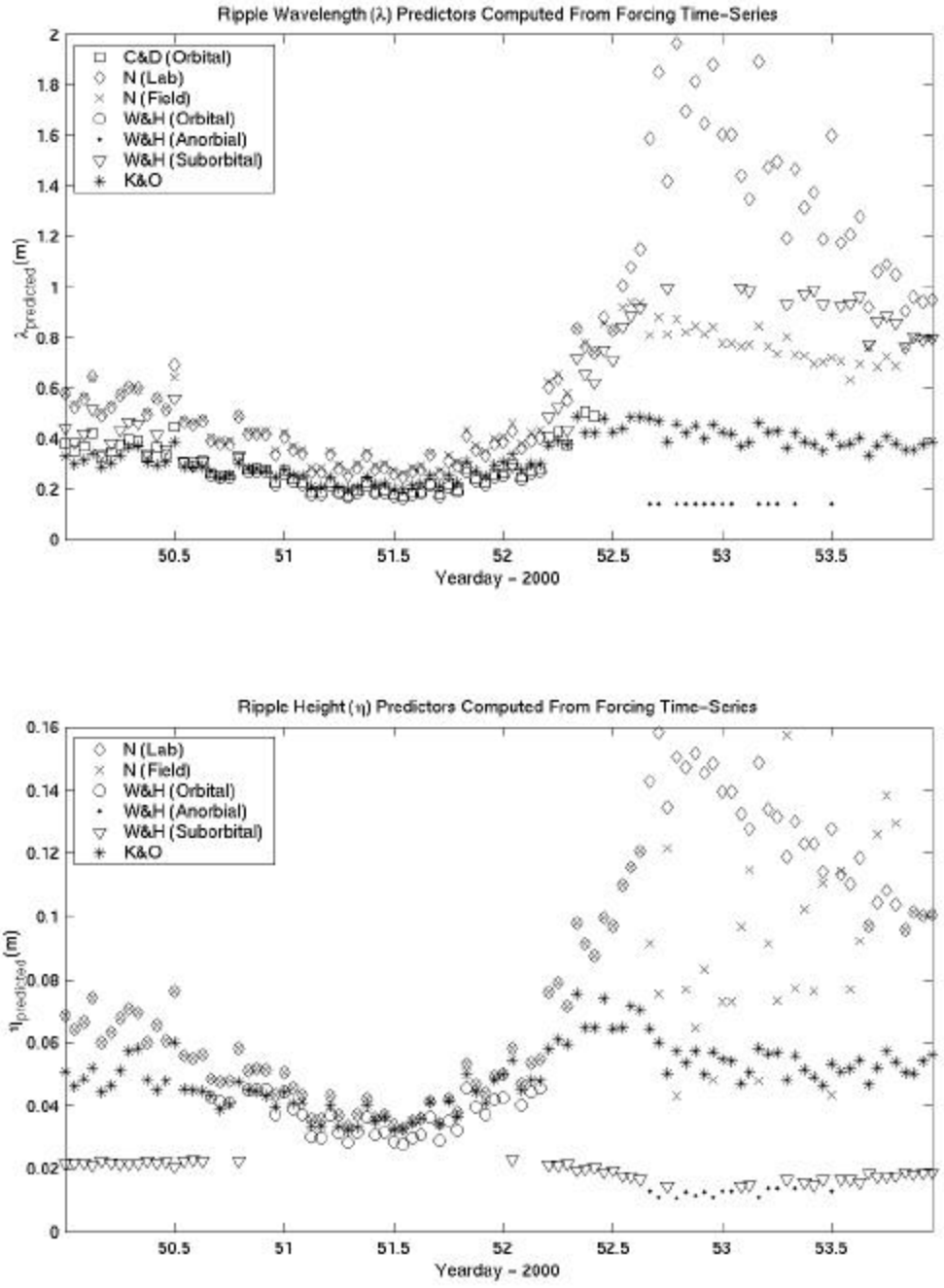

Figure 29. Bed response algorithms for (a) ripple wavelength, and (b) ripple height according to C&D – Clifton and Dingler [1984], N - Nielsen [1981], W&H – Wiberg and Harris [1994], and Khelifa and Oullet [2000] for days 50-54.

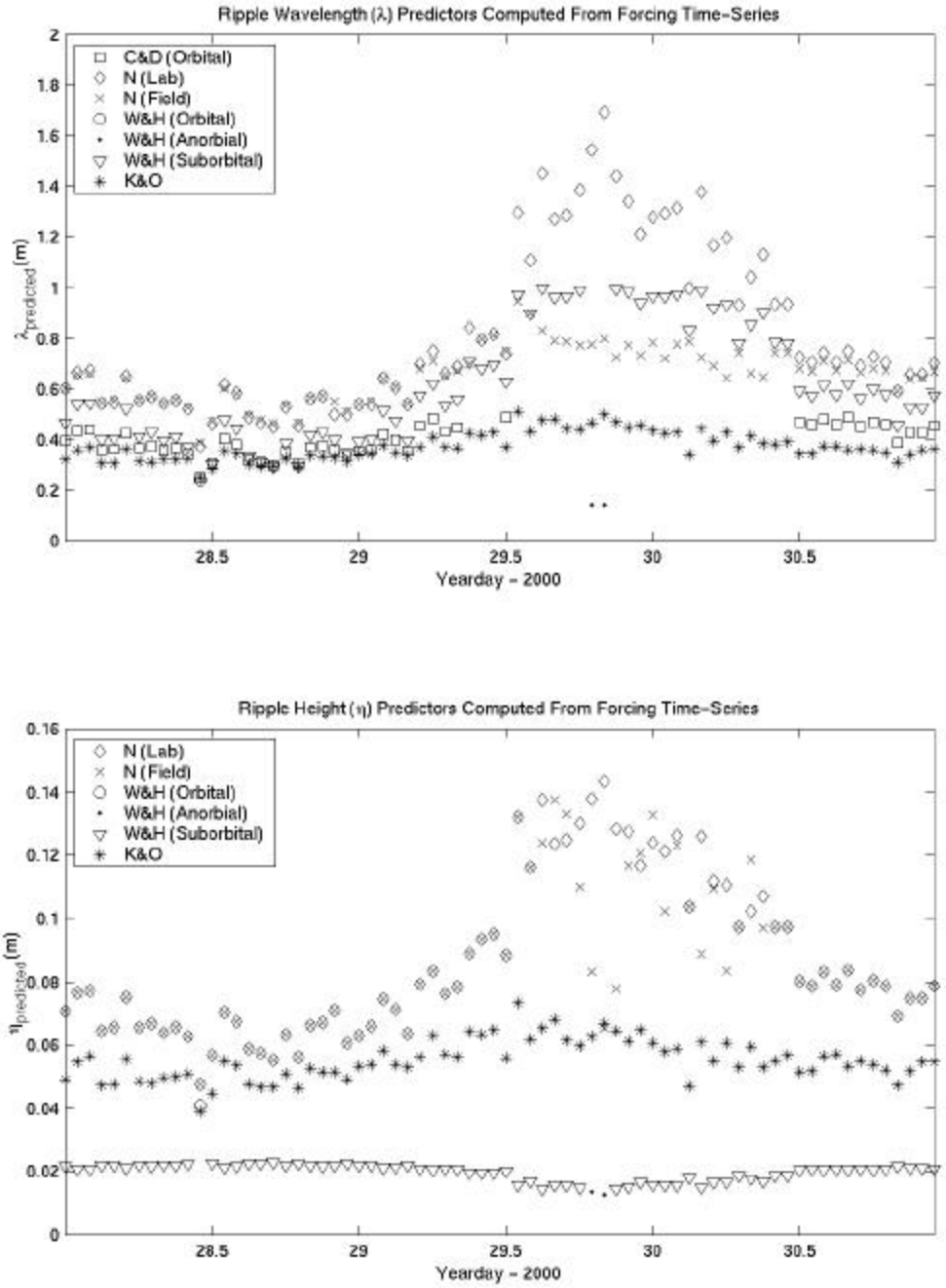

Figure 30. Bed response algorithms for (a) ripple wavelength, and (b) ripple height according to C&D – Clifton and Dingler [1984], N - Nielsen [1981], W&H – Wiberg and Harris [1994], and Khelifa and Oullet [2000] for days 28-31.

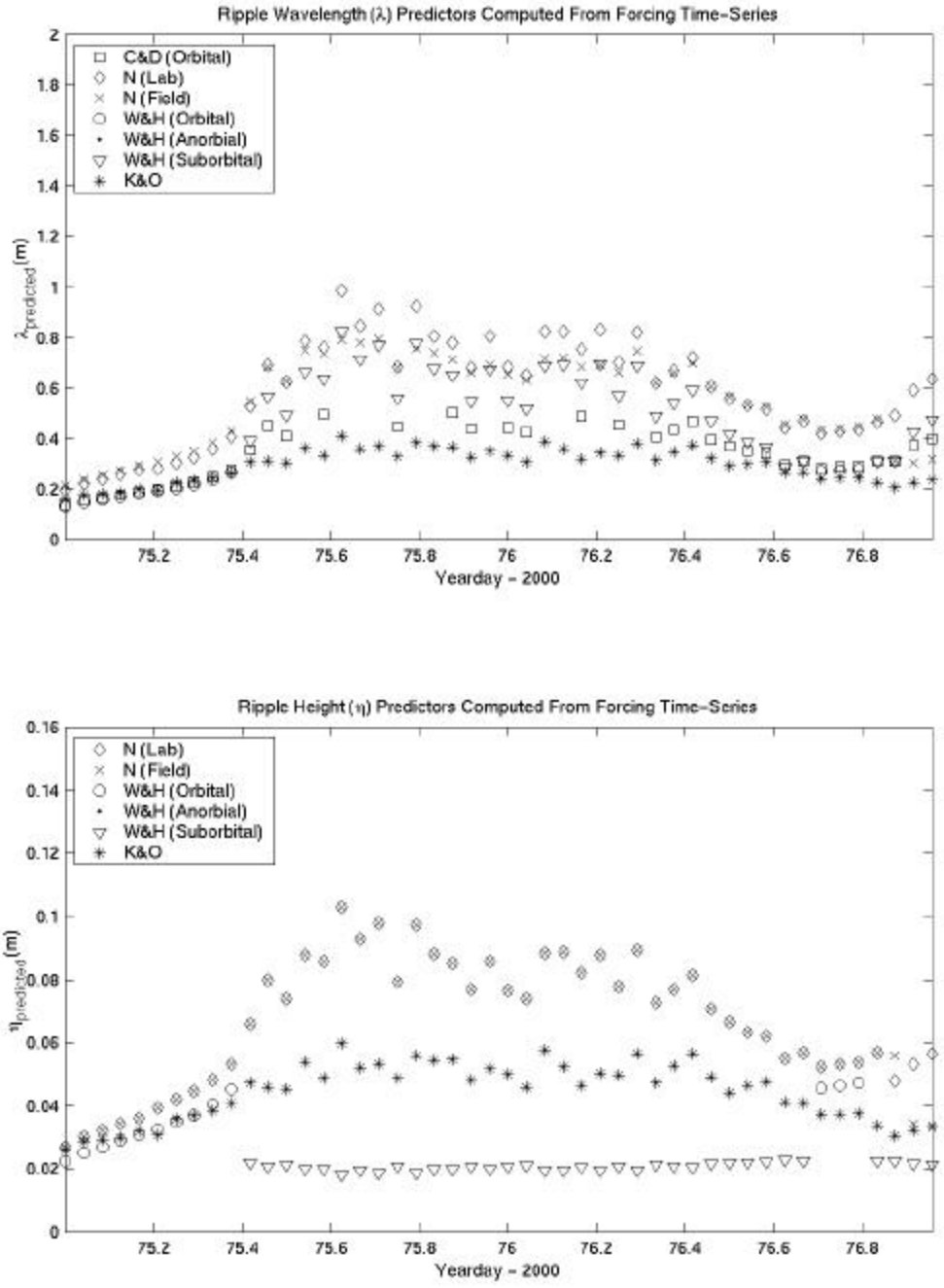

Figure 31. Bed response algorithms for (a) ripple wavelength, and (b) ripple height according to C&D – Clifton and Dingler [1984], N - Nielsen [1981], W&H – Wiberg and Harris [1994], and Khelifa and Oullet [2000] for days 75-77.

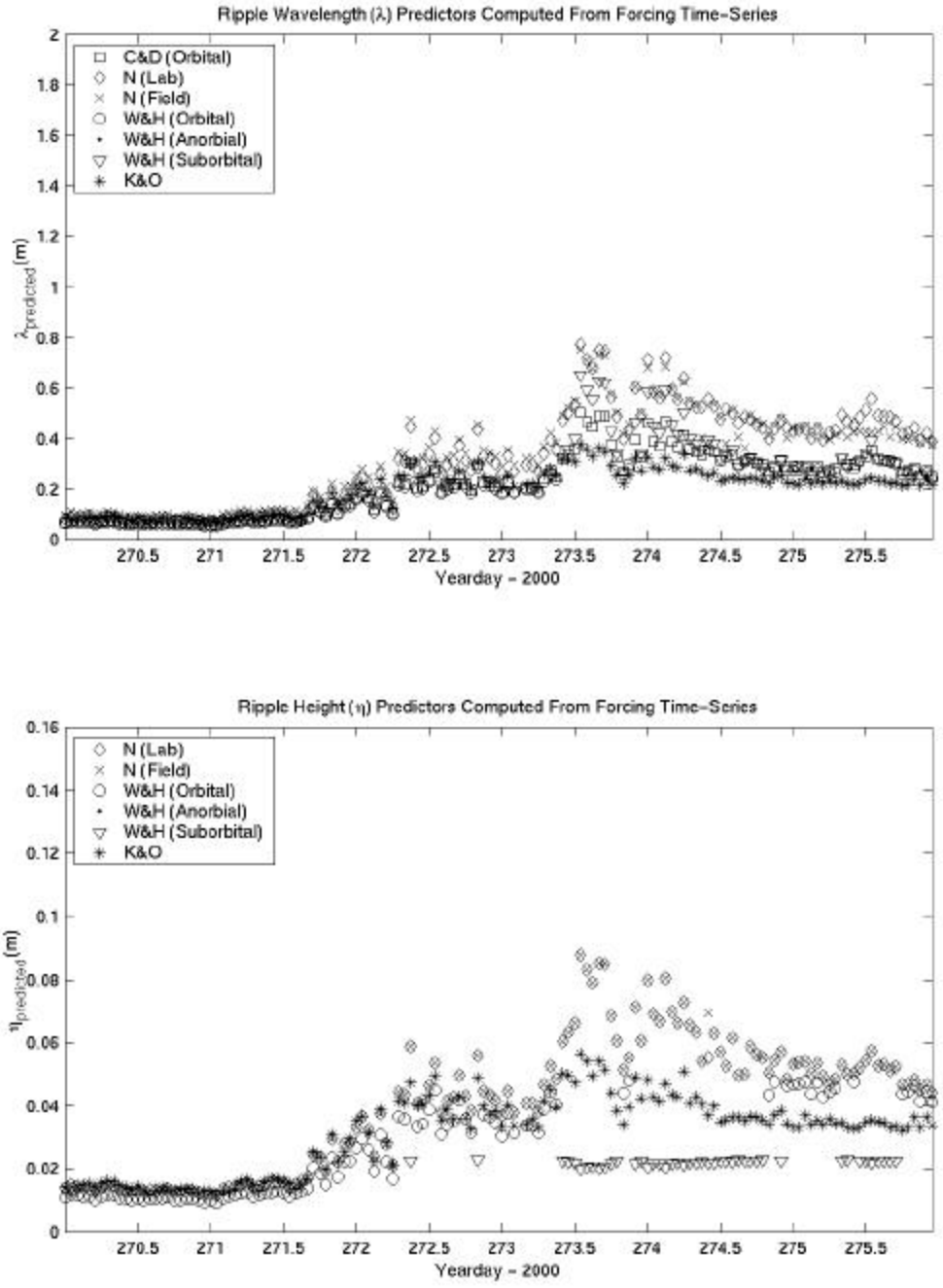

Figure 32. Bed response algorithms for (a) ripple wavelength, and (b) ripple height according to C&D – Clifton and Dingler [1984], N - Nielsen [1981], W&H – Wiberg and Harris [1994], and Khelifa and Oullet [2000] for days 270-276.

THIS PAGE INTENTIONALLY LEFT BLANK

V. CONCLUSION

The analysis of bedform evolution under combined wave and current forcing at the nearshore MISO site has detected a significant amount of ripple evolution in the alongshore direction. It has been demonstrated that the bed is dominated by relict ripples remaining from previously formed ripples as the forcing decreased below critical flow requirements. As the combined flow increased above critical, a rapid transition from alongshore to cross-shore bedform evolution was observed as the bedforms adjusted to new active forcing. The resulting ripple growth was not wave direction oriented.

Using the bed geometry and wave and current forcing time-series, it has been demonstrated that upon comparison of several laboratory and field derived models, *Khelifa and Oullet* [2000] provided substantially better estimates of ripple wavelength, even during periods of alongshore growth. *Nielsen's* [1981] predictors greatly overestimated bed response, while the *Wiberg and Harris'* [1994] suborbital model performed adequately during periods of cross-shore ripple growth.

To better understand the conditions resulting in alongshore ripple growth and account for this growth not being adequately predicted by laboratory models, an on-going investigation will examine contributions from mean currents, infragravity energy, reflected wave energy, and wave asymmetries. Statistical analysis of these time-series may yield important insight into the development of ripples contrary to the orientation of wave orbital velocities.

THIS PAGE INTENTIONALLY LEFT BLANK

APPENDIX

To calculate the directional spectra of incoming waves at the MISO site, a Maximum Entropy Method (MEM) directional wave spectra algorithm was applied to pressure (p), cross-shore (u) and alongshore (v) velocity time-series. The procedure utilized is based on *de Valk* [1990] and *Rockafellar* [1974]. First, cross-spectral densities are obtained. These cross-spectral densities can be viewed as

$$f_1 = \langle pp \rangle \tag{A1}$$

$$f_2 = \langle pu \rangle \sim pp \cos\theta \tag{A2}$$

$$f_3 = \langle pv \rangle \sim pp \sin\theta \tag{A3}$$

$$f_4 = \langle uu \rangle \sim pp \cos^2\theta \tag{A4}$$

$$f_5 = \langle vv \rangle \sim pp \sin^2\theta \tag{A5}$$

$$f_6 = \langle uv \rangle \sim pp \sin\theta \cos\theta \tag{A6}$$

Using sinusoidal identities,

$$f_4 - f_5 \sim pp\left|\cos^2\theta - \sin^2\theta\right| = pp \cos 2\theta \tag{A7}$$

$$2f_6 \sim pp 2 \sin\theta \cos\theta = pp \sin 2\theta \tag{A8}$$

Normalizing the Fourier components A1-A3 and A7-A8 according to *Long* [1980] yields

$$f_1' = 1 \tag{A9}$$

$$f_2' = \frac{f_2}{f_1\sqrt{f_2 + f_3}} \tag{A10}$$

$$f_3' = \frac{f_3}{f_1\sqrt{f_2 + f_3}} \tag{A11}$$

$$f_4' = \frac{f_4 - f_5}{f_4 + f_5} \tag{A12}$$

$$f_5' = \frac{2f_6}{f_4 + f_5} \tag{A13}$$

To calculate the entropy of system (*E(q)*) as a function of the directional distribution (*D*) on (-π,π), let

$$E(q) = -\int_{-p}^{p} D\ln(D)dq \tag{A14}$$

In order to maximize the entropy of this system while keeping it constrained by the measured quantities (normalized spectral values, $f'_{n,}$ calculated in A9-A13), the equation

$$\int_{-p}^{p} D(q)\exp(inq)dq - f_n' = 0 \tag{A15}$$

must be satisfied. Introducing the Lagrangian multipliers m_n yields

$$F = \int_{-p}^{p} \left[-D(q)\ln(D(q)) - \sum_n m_n D(q)\exp(inq) \right] dq + \sum_n m_n f_n = 0 \qquad \text{(A16)}$$

Maximizing F with respect to D (i.e. maximizing the entropy) produces the equation

$$\frac{dF}{dD} = \int_{-p}^{p} \left[-1 - \ln(D(q)) - \sum_n m_n \exp(inq) \right] dq = 0 \qquad \text{(A17)}$$

where

$$\ln(D(q)) = -1 - \sum_n m_n \exp(inq) \qquad \text{(A18)}$$

and the definition of directional distribution is

$$D(q) = \exp\left[-1 - \sum_n m_n \exp(inq) \right] \qquad \text{(A19)}$$

Substituting D (A19) into F (A16),

$$\begin{aligned} q = \int_{-p}^{p} - \exp\left[-1 - \sum_n m_n \exp(inq) \right] * \left[-1 - \sum_n m_n \exp(inq) \right] \ldots \\ + \sum_n m_n \exp\left[-1 - \sum_n m_n \exp(inq) \right] \exp(inq) dq + \sum_n m_n f_n \end{aligned} \qquad \text{(A20)}$$

and simplifying

$$q = \int_{-p}^{p} \exp\left[-1 - \sum_n m_n \exp(inq)\right] dq + \sum_n m_n f_n \qquad \text{(A21)}$$

To maximize q as a function of the Lagrangian multipliers, this equation is solved by the BFGS Quasi-Newton method with a mixed quadratic and cubic line search procedure (*Broyden, 1970* and *Shanno, 1970*).

Applying the linear dispersion relationship and a linear theory wave transfer function

$$H(k) = \left(\frac{\cosh(kh)}{\cosh(kz)}\right)^2 \qquad \text{(A22)}$$

where k is the wavenumber ($2p/l$), h is the local water depth, and z is the depth of measurement, to the maximized directional distribution multiplied by the cross-spectral densities produces the wave directional spectral estimates corrected to the surface elevation. From this quantity, the peak frequency (or period), peak wave direction, mean wave direction, and spectral width can be calculated.

LIST OF REFERENCES

Amos, C.L., A.J. Bowen, D.A. Huntley, and C.F.M. Lewis, Ripple generation under the combined influences of waves and currents on the Canadian continental shelf, *Continental Shelf Research, 8*(10), 1129-1153, 1988.

Bagnold, R.A., Motion of waves in shallow water: Interaction between waves and sand bottoms, *Proceedings of the Royal Society of London, Series A, 187*, 1-15, 1946.

Boyd, R., D.L. Forbes, and D.E. Heffler, Time-sequence observations of wave-formed sand ripples on an ocean shoreface, *Sedimentology, 35*, 449-464, 1988.

Broyden, C.G., The convergence of a class of double-rank minimization algorithms, *Journal of the Institute of Mathematics and its Applications, 6*, 76-90, 1970.

Clifton, H.E., and J.R. Dingler, Wave-formed sedimentary structures and paleoenvironmental reconstruction, *Marine Geology, 60*, 165-198, 1984.

de Valk, C., Algorithms for estimation of spectra from sea surface imagery, *WL|Delft Hydraulics report H467*, 1990.

Deigaard, R., P. Justesen, and J. Fredsoe, Modeling of undertow by a one-equation turbulence model, *Coastal Engineering, 15*, 431-458, 1991.

Dingler, J.R., Wave-formed ripples in nearshore sands, P.h.D. thesis, 136 pp., Univ. of Calif., San Diego, 1974.

Glenn, S.M., and W.D. Grant, A suspended sediment stratification correction for combined wave and current flows, *Journal of Geophysical Research, 92*, 8244-8264, 1987.

Grant, W.D., and O.S. Madsen, Combined wave and current interaction with a rough bottom, *Journal of Geophysical Research, 84*, 1797-1808, 1979.

Grant, W.D., and O.S. Madsen, Movable bed roughness in unsteady oscillatory flow, *Journal of Geophysical Research, 87*, 469-481, 1982.

Hay, A.E., and D.J. Wilson, Rotary sidescan images of nearshore bedform evolution during a storm, *Marine Geology, 119*, 57-65, 1994.

Jonsson, I.G., Wave boundary layers and friction factors, *Proceedings 10th Coastal Engineering Conference, 1*, 127-146, 1966, American Society of Civil Engineers, New York, 1967.

Khelifa, A., and Y. Oullet, Prediction of sand ripple geometry under waves and currents, *Journal of Waterway, Port, Coastal, and Ocean Engineering, 126*, 14-22, 2000.

Li, M.Z., and C.L. Amos, Predicting ripple geometry and bed roughness under combined waves and currents in a continental shelf environment, *Continental Shelf Research, 18*, 941-970, 1998.

Longuet-Higgins, M.S., and R.W. Stewart, Radiation stress and mass transport in gravity waves, with applications to surf beats, *Journal of Fluid Mechanics, 13*, 481-504, 1962.

Miller, M.C. and P.D. Komar, Oscillation sand ripples generated by laboratory apparatus, *Journal of Sedimentary Petrology, 50*(1), 173-182, 1980(a).

Miller, M.C. and P.D. Komar, A field investigation of the relationship between oscillation ripples spacing and the near-bottom water orbital motions, *Journal of Sedimentary Petrology*, 50(1), 183-191, 1980(b).

Mogridge, G.R. and J.W. Kamphuis, Experiments on bedform generation by wave action, *Coastal Engineering, Proceedings of the 13th Conference.*, pp. 1123-1142, American Society of Civil Engineers, New York, 1972.

Nielsen, P., Dynamics and geometry of wave-generated ripples, *Journal of Geophysical Research, 86*, 6467-6472, 1981.

RDI, Workhorse Acoustic Doppler Current Profiler Technical Manual, *Technical Manual*, 1998.

Rockafellar, R.T., Conjugate duality and optimization, Society for Industrial and Applied Mathematics, Philadelphia, 1974.

Shanno, D.F., Conditioning of quasi-Newton methods for function minimization, *Mathematics of Computing, 24*, 647-656, 1970.

Shi, N.C., and L.H. Larsen, Reverse sediment transport induced by amplitude modulated waves, *Marine Geology, 54*, 181-200, 1984.

Stanton, T.P., www.oc.nps.navy.mil/~stanton/miso, 1999.

Stanton, T. P., Characterizing wave-forced bedforms using a two axis scanned acoustic altimeter. Submitted to of Atmospheric and Oceanic Technolology, 2000.

Traykovsky, P., A.E. Hay, J.D. Irish, and J.F. Lynch, Geometry, migration, and evolution of wave orbital ripples at LEO-15, *Journal of Geophysical Research, 104*, 1505-1524, 1999.

Wheatcroft, R.A., Temporal variation in bed configuration and one-dimensional roughness at the mid-shelf STRESS site, *Continental Shelf Research, 14*(10/11), 1167-1190, 1994.

Wiberg, P.L., and C.K. Harris, Ripple geometry in wave-dominated environments, *Journal of Geophysical Research, 99*, 775-789, 1994.

Yalin, M.S., and R.C. Russell, Similarity in sediment transport due to waves, *Coastal Engineering*, Proc. 8th Conf., Mexico City, 1962, 151-167, Council on Wave Research, Richmond, California, 1963.

THIS PAGE INTENTIONALLY LEFT BLANK

INITIAL DISTRIBUTION LIST

1. Defense Technical Information Center
   Ft. Belvoir, Virginia

2. Dudley Knox Library
   Naval Postgraduate School
   Monterey, California

3. Dr. Mary L. Batteen
   Chairman
   Department of Oceanography
   Naval Postgraduate School
   Monterey, California

4. Professor Tim Stanton
   Department of Oceanography
   Naval Postgraduate School
   Monterey, California

5. Dr. Edward B. Thornton
   Department of Oceanography
   Naval Postgraduate School
   Monterey, California

6. Mr. James A. Stockel
   Department of Oceanography
   Naval Postgraduate School
   Monterey, California

7. Mr. Robert M. Wyland
   Department of Oceanography
   Naval Postgraduate School
   Monterey, California

8. Dr. Ad T. Reniers
   Department of Oceanography
   Naval Postgraduate School
   Monterey, California

9. CDR Arthur R. Parsons, USN
   Department of Oceanography
   Naval Postgraduate School
   Monterey, California

10. Dr. Clyde L. Scandrett
Department of Mathematics
Naval Postgraduate School

11. CAPT Dennis J. Whitford, USN
Oceanography Department
United States Naval Academy
Annapolis, Maryland

12. Dr. Mario Vieira
Oceanography Department
United States Naval Academy
Annapolis, Maryland

13. CDR Henry Jones, USN
Oceanography Department
United States Naval Academy
Annapolis, Maryland

14. LCDR Michiko J. Martin, USN
Oceanography Department
United States Naval Academy
Annapolis, Maryland

15. Dr. Virginia Smith
Chemistry Department
United States Naval Academy
Annapolis, Maryland

16. Dr. Daniel W. O'Sullivan
Chemistry Department
United States Naval Academy
Annapolis, Maryland

17. Dr. Clarence L. Baugh
Custom Biologicals, Inc.
902 Clint Moore Road, Suite #208
Boca Raton, FL 33487

18. Dr. David M. Binninger
Department of Biological Sciences
Florida Atlantic University
Boca Raton, FL 33431

19. Mr. William C. Blodgett, SR
798 Blueberry Dr.
Wellington, FL 33414